Chair of Functional Materials and Materials Systems

Master's Thesis

Thermal expansion of sputter-deposited Ti(C,N) determined by high temperature X-ray diffraction

November 2018

Christoph Kickinger, BSc

Acknowledgment

Great thanks go to Univ.-Prof. DI Dr. Christian Mitterer, Head of the Department of Physical Metallurgy and Materials Testing, for giving me the opportunity to execute this work at his department and delve into the field of hard coatings.

I am very grateful to my supervisor DI Dr. Christian Saringer for the advices he gave me during the execution of my work, for correcting this thesis with such patience, always having an open ear for my problems and most important, showing me the best place for picking Swiss stone pine cones.

Many thanks go to DI Dr. Nina Schalk, Head of the Christian Doppler Laboratory for Advanced Coated Cutting Tools and DI Dr. Michael Tkadletz, for the confidence in admitting me in their group and the interesting discussions we had together.

I would also like to thank Sabrina Hirn and Mag. Velislava Terziyska for helping me producing the materials for my thesis in such a friendly and careful way and of course for the tasty pumpkins.

Furthermore, I want to say thanks to all my colleagues at the chair of Functional Materials and Materials Systems for helping me in any case and making my time there to an unforgettable and very funny memory.

My final thanks are to my parents and friends, who supported and helped me during my whole studies and so enabled all this for me.

Affidavit

I declare in lieu of oath, that I wrote this thesis and performed the associated research myself, using only literature cited in this volume.

Leoben, 11/08/2018

Contents

1 Introduction

Cutting tools like drills and cutting inserts are exposed to many different types of wear during application. From adhesion over abrasion to oxidational wear, many effects can harm the surface of the tools and thus their performance [1]. To counter these effects, a multitude of different coatings has been developed, deposited by several techniques like e.g. sputtering or cathodic arc evaporation [2, 3]. These coatings commonly consist of a base layer, deposited directly onto the substrate and a top layer. Between the base and the top layer often one or more interlayers are placed [4]. Top layers are used to improve the hardness and friction behavior, as well as to enhance the oxidation resistance, resulting in better wear resistance [5–8]. Intermediate or base layers are typically used to increase the adhesion between the substrate and other layers, to compensate thermal mismatches or to act as diffusion barrier [9, 10]. For both application areas described, the thermal expansion is a crucial factor of the layers, both during deposition and operation. For the deposition, often high temperatures up to several hundred °C are needed and so high stresses and subsequent cracks can occur during cooling. This is especially the case, if the thermal expansion between the substrate and the coating or between the different layers exhibits a high mismatch. During operation it is also highly important to adjust the thermal expansion of the layers and the difference to the substrate, as the profitability of cutting processes can strongly be increased by increasing the cutting speed. This increase consequently raises the surface temperatures of the tools and thus can result in thermal stresses and subsequent cracks in the coating, as well as delamination [11–13] .

A coating system, which exhibits big advantages in enhancing the cutting performance and lifetime of cutting tools, either as top or as base layer, is Ti(C,N) [3]. It not only shows high hardness and good wear resistance, but also excellent adhesion to steel compared to pure TiN and TiC [7]. Depending on the desired characteristics and the field of application, the coating composition can vary from pure TiN to pure TiC, which allows the variation of the properties, like e.g. the hardness, the oxidation behavior and the thermal expansion coefficient (TEC) [7, 8]. This is possible because of the complete solubility within the TiN-TiC system, where the [C]/[C+N] ratio can vary from zero to one [14, 15].

Thus, the aim of this thesis is the determination of the TEC of Ti(C,N) as a function of temperature and chemical composition. Ti(C,N) coatings with eleven different compositions

ranging from pure TiN to pure TiC were deposited by nonreactive, unbalanced magnetron sputter deposition. Afterwards the coatings were powdered and measured by X-ray diffraction (XRD) in a high temperature (HT) chamber between 25 and 1000 °C. From the X-ray diffractograms, the lattice constants at the different temperatures and further on the thermal expansion coefficients were determined, by refining the lattice parameters based on the space group of Ti(C,N). To obtain reliable temperatures, related to the measured lattice constants, the HT chamber was calibrated before the measurements by three different methods. With these data a calibration curve was calculated, which was used to correct the recorded temperatures for Ti(C,N) in order to diminish the error of the lattice parameter determinations.

2 Theoretical background

2.1 Magnetron sputtering

Since several decades magnetron sputtering is a commonly used method for deposition of coatings with thicknesses up to some µm [16]. It belongs to the group of physical vapor deposition (PVD) methods, which are based on the physical transfer of solid material to the vapor phase and subsequent deposition on a substrate by condensation. Using PVD techniques, a variety of different substrates, ranging from metals over ceramics to plastics, can be coated [17]. Sputtering is based on the ionization of process gas atoms, usually Ar, by collisions with electrons generated by a glow discharge, which is resulting in so called plasma. The electrons are accelerated by an electric field between a negatively biased electrode, called target and a high vacuum chamber as grounded electrode, wherein the process takes place. The ionized atoms are accelerated towards the target, which is consisting of the desired coating material, where target atoms are transferred to the vapor phase by energy and momentum transfer. These vaporized atoms then condense on the substrate, forming the coating. The electrons are created mostly as a result of the ionization of the gas atoms, but also in form of secondary electrons at the target surface [17, 18].

In order to enhance the collisions of electrons and gas atoms and consequently the ionization events, the electrons can be concentrated above the target using a magnetic field. This is achieved by the installation of permanent magnets behind the target, creating a so-called magnetron [16–18]. The basic effect of a magnetron is that due to the crossing of the magnetic and the electric field the Lorentz force traps the electrons above the target, consequently increasing the collision probability of electrons and atoms [18, 19].

Generally, the sputtering rates are considerably increased when a magnetron is used. In addition to higher deposition rates, magnetron sputtering has the advantage that due to the localized plasma lower substrate heating effects occur, which makes it possible to hold the substrate temperature low during deposition. Furthermore, the increased ionization efficiency allows for approximately 10 times lower operating pressures and operating voltages than without magnetrons. Due to the lower pressures, the number of collisions of vaporized target atoms and process gas atoms is decreased, also contributing to higher deposition rates [19, 20].

A magnetron can be distinguished by the alignment of the magnets into balanced and unbalanced magnetrons. The difference is, that in balanced configuration the outer and the inner magnets have the same strength and so all magnetic field lines are closed, leading to a negligible ion current at the substrate. In unbalanced magnetrons, however, either the outer or the inner magnets are stronger and therefore some of the field lines are extended to the substrate. This alignment causes that several of the electrons are moving towards the substrate and ionizing Ar atoms on their way, resulting in substrate ion current densities up to 10 mA/cm². Thus, an increase in current of one order of magnitude can be achieved compared to balanced magnetrons [20–22]. The resulting ion bombardment of the substrate strongly affects the properties of the deposited film, like density, residual stress or microstructure [20]. This effect can even be increased by applying a bias voltage to the substrate, which additionally accelerates the Ar ions, enabling a tailoring of the coating properties [20].

In addition, magnetron sputtering can be divided into two different modes depending on the process gas used, i.e. reactive and nonreactive sputtering. The difference is that nonreactive sputtering uses an inert process gas, which does not react with the target material and thus only vaporizes the target. In reactive sputtering mode, however, additionally a reactive gas like for instance nitrogen or oxygen is introduced, which reacts with the target atoms and therefore becomes incorporated in the deposited coating [17, 18].

Figure 1 shows a planar, circular magnetron setup using Ar as process gas in unbalanced configuration, comparable to the configuration used in this work. In this example the magnetic field lines are directed from the outer region of the target to the inner.

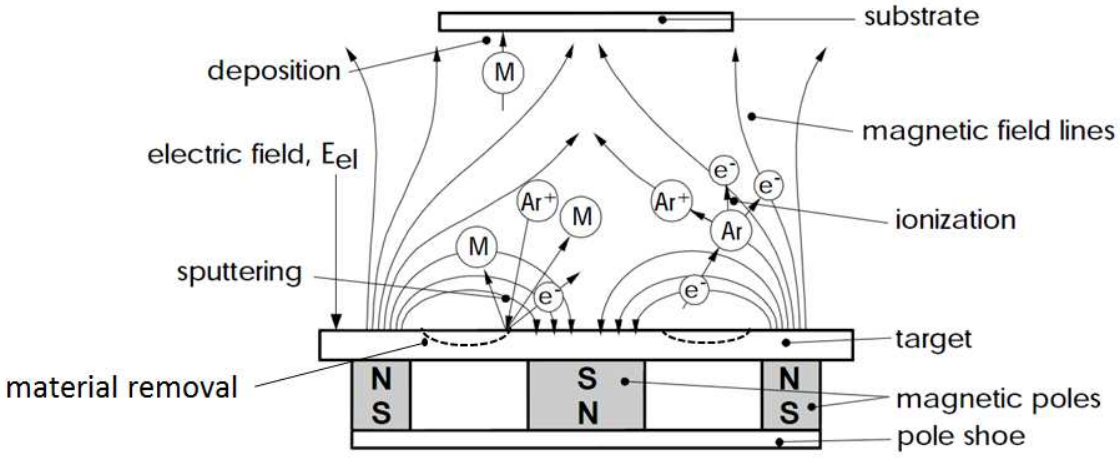

Figure 1: Set up of an unbalanced, planar, circular magnetron in nonreactive mode [23].

2.2 The Ti(C,N) coating system

2.2.1 General properties and structure of Ti(C,N)

Various compositions of Ti(C,N) are commonly applied as hard and wear resistant coatings to improve lifetime of cutting tools [5]. They can be used as top, intermediate, or base layers, either to provide hardness and wear resistance or the adhesion of other layers [6]. Also a coloring from gold over bronze to grey can be achieved, depending on the chemical composition [24].

Ti(C,N) coatings have been extensively investigated in the past with respect to hardness, wear resistance, friction and oxidation behavior, as well as to the adhesion on different substrates [5–8, 25]. It was found that the hardness shows an approximately linear increase with increasing C content from pure TiN to pure TiC [25]. This is in good agreement with the wear resistance, which shows the same dependency [6]. A characteristic of physical vapor deposited Ti(C,N) coatings is that they exhibit higher hardness and therefore better wear resistance than those deposited with chemical vapor deposition (CVD) techniques [5]. For optimizing the properties of the coating not only the chemical composition of the carbonitrides is decisive, the microstructure and the architecture of the coating are also crucial factors. Often the C content exhibits a gradient over the layer thickness, or the coating consists of several sublayers mixed with other layers to enhance the properties, e.g. a Ti(C,N), Ti(Nb,C,N) multilayered coating to increase the hardness [26–28].

The structure of Ti(C,N) can be divided in three different models. In the first model Ti, C and N atoms are completely randomly distributed in a face centered cubic (fcc) structure (Fig. 2a) [29]. The other models consist of a fcc-structure, similar to TiN where only the C and N atoms are randomly exchanged (Fig. 2b) [30] or more complex tetragonal structures with full order of the atomic arrangement (Fig. 2c) [31]. By a comparison of the different structures using Rietveld refinement of X-ray powder diffraction data, Levi *et al.* showed that the structure of Ti(C,N) is most likely based on the TiN structure (NaCl type), where the N atoms are substituted randomly by C atoms with only a small number of vacancies (Fig. 2b) [31].

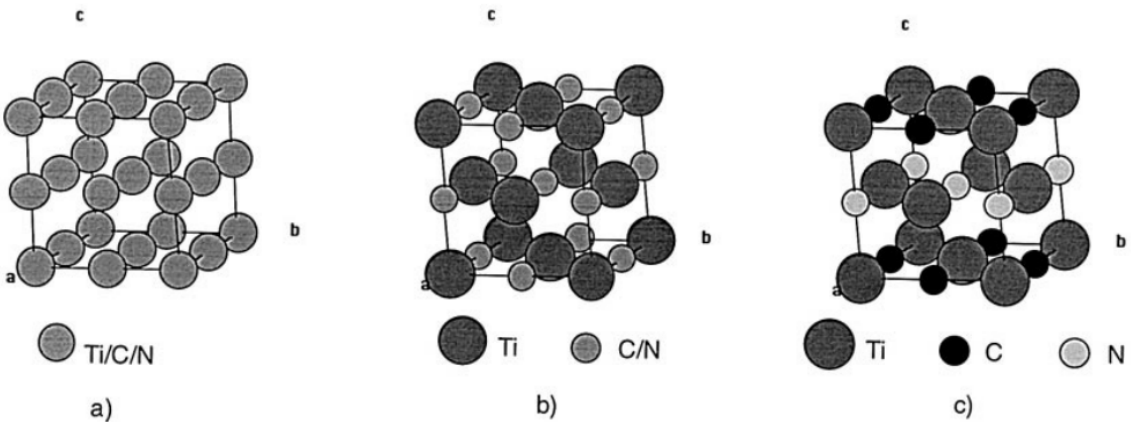

Figure 2: Different possible structure models of Ti(C,N) [31].

The exchange of N and C is in good agreement with the phase diagram of TiC and TiN, which exhibits a complete solubility over the whole compositional range [14, 15, 32].

The lattice parameters of pure TiN and TiC at room temperature are 4.2417 Å [33] and 4.3280 Å [34], respectively. It could be shown by Schneider *et al.*, that the lattice parameter of Ti(C,N) rises with increasing C content roughly linear [35], showing a Vegard's-like behavior [36]. However, when studying sputtered coatings it can be found, that the lattice constant is generally higher than that of bulk materials. This is depending on the deposition parameters like the bias voltage and the temperature, affecting the residual stress, as well as on the layer thickness and the microstructure of the coating [37–39]. The reasons for the variation of the lattice constant are explicated by Sundgren as follows [40]:

- Ar incorporations into the sputtered films result in increased residual stress.
- Differences in thermal expansion coefficients of the film and the substrate cause thermal stress.
- Impurities like O lead to a decrease of the lattice parameter.
- A high density of grain boundaries and defects lead to residual stresses.
- Incorporation of N interstitially in tetrahedral positions leads to an expansion of the lattice.

Despite the high effort in improving Ti(C,N) coatings with respect to hardness, friction and corrosion, there is only little knowledge about the thermal properties, especially on the thermal expansion of Ti(C,N).

2.2.2 Thermal expansion of Ti(C,N)

For powder-metallurgically produced TiN and TiC with N/Ti and C/Ti ratios of 0.95, the thermal expansion was studied by Houska [41]. He stated, that TiN as well as TiC exhibit a linear thermal expansion up to 1419 °C and 2080 °C, respectively, starting from 25 °C. For comparison, TiN has an expansion of 0.850 % at 1011 °C and TiC of 0.785 % at 1016 °C related to 25 °C. Thus, TiN shows a higher increase in lattice parameter than TiC, resulting from a higher atomic vibration amplitude.

A determination of the thermal expansion by HT XRD over the whole range of hot pressed Ti(C,N) from TiC to TiN was done by Aigner *et al.* [42]. The lattice parameter in the temperature range of 298-1473 K can be calculated using eq. 1

$$a_{\left(\frac{[C]}{[C]+[N]},T\right)} = 0.42313 + 0.0088 \cdot \frac{[C]}{[C]+[N]} + \left(2.338 - 0.122 \cdot \frac{[C]}{[C]+[N]}\right) \cdot T \cdot 10^{-6} + \left(1.0717 - 0.2258 \cdot \frac{[C]}{[C]+[N]}\right) \cdot 10^{-9} \cdot T^2 \pm 0.0002\ nm\ , \quad (1)$$

where *[C]* and *[N]* are the atomic percentages of C and N and *T* is the absolute temperature in K. The average TEC α_{av} in the temperature range written above is calculated by

$$\alpha_{av\left(\frac{[C]}{[C]+[N]}\right)} = \left(9.9 - 1.4 \cdot \frac{[C]}{[C]+[N]}\right) \cdot 10^{-6}\ K^{-1} \quad (2)$$

and the linear TEC α by

$$\alpha_{\left(\frac{[C]}{[C]+[N]},T\right)} = \frac{\left(2.338-0.122\cdot\frac{[C]}{[C]+[N]}\right)\cdot 10^{-6}+\left(2.143+0.451\cdot\frac{[C]}{[C]+[N]}\right)\cdot 10^{-9}\cdot T}{a_{\left(\frac{[C]}{[C]+[N]},T\right)}} K^{-1}. \quad (3)$$

Figure 3 shows the linear thermal expansion reported by Aigner *et al.* [42] over the specified temperature range of five different compositions compared with the values for TiN and TiC determined by Houska [41]. In general, in both studies the same trend of a rising TEC with increasing N content was found. Using *ab initio* calculations for five different compositions, from TiN to TiC, Kim *et al.* could also confirm this trend [43]. They developed different polynomials up to the fourth degree for calculating the linear TEC, depending on the temperature range. Wokulska studied the temperature influence on the expansion of Ti(C,N) whiskers and also found a good correlation of the lattice parameter with those reported in ref. [42] for the temperature range of 275 to 630 K [44].

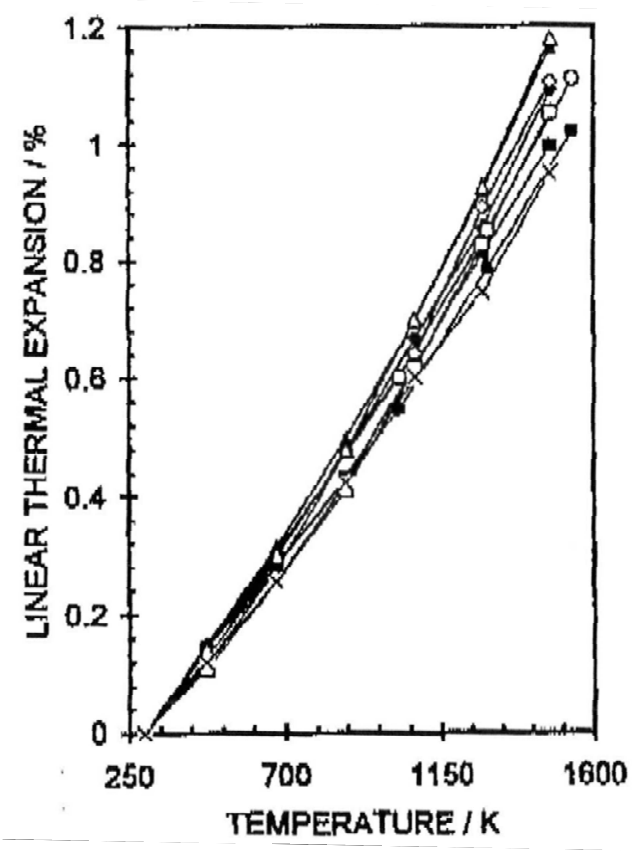

Figure 3: Linear thermal expansion of TiC_xN_{1-x} [42]: ■ TiC, □ TiN, ◆ $TiC_{0.6}N_{0.4}$, ◇ $TiC_{0.4}N_{0.6}$, ▲ $TiC_{0.2}N_{0.8}$, △ TiN, ● TiC [41], ○ TiN [41], x TiC

Due to the linear increase in lattice parameter in the defined temperature range, α is temperature independent according to

$$\alpha = \left\{9.40 - 6.47 \cdot \left[\frac{C}{C+N}\right] + 5.72 \cdot \left[\frac{C}{C+N}\right]^2\right\} \cdot 10^{-6}\ K^{-1}. \quad (4)$$

The dependence of α on the chemical composition of Ti(C,N) is presented in Fig. 4. It can be seen that α of TiN is higher than that of TiC with a significant decrease for the ternary Ti(C,N). $TiC_{0.6}N_{0.4}$ had the lowest value of α [44], which is an indication for dominating Ti-C bonds in the crystals of Ti(C,N) solid solutions.

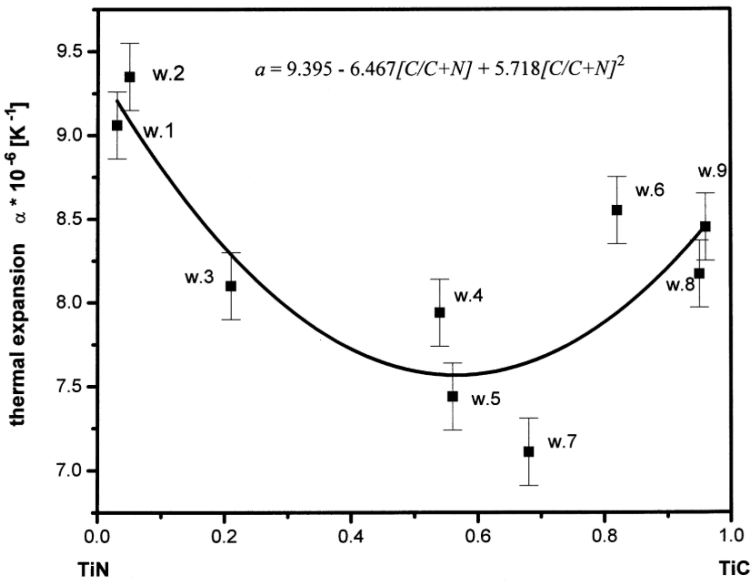

Figure 4: TEC as a function of the composition of Ti(C,N) valid for a temperature range from 275 to 630 K [44].

When investigating the thermal properties at elevated temperatures in O_2 containing atmosphere, the oxidation behavior has to be taken into account. As shown by Zhang *et al.* on the basis of TiN, Ti-based ceramic coatings form TiO_2 when oxidized [45]. The oxidation resistance of Ti(C,N) coatings was mostly analyzed by means of wear resistance testing. It has been shown, that the wear rate rises due to oxidation at temperatures exceeding 300 °C [46]. Other studies report that the highest oxidation temperature, at which the coating retains its surface morphology, varies from 500 to 600 °C depending on the chemical composition of the Ti(C,N) [47].

2.3 X-ray diffraction and Rietveld refinement

2.3.1 X-ray diffraction

For the analysis of the crystallographic structure of materials, XRD is a commonly used method. It is based on the diffraction of electromagnetic waves at the lattice planes of crystals, according to Bragg`s law (eq. 5) [48]. This law states, that the diffracted waves show constructive interference, when two times the lattice distance times the sine of the Bragg angle θ_B is equal to *n* times the wavelength λ of the incoming beam, where *n* is the order of the reflection [48]:

$$n \cdot \lambda = 2 \cdot d \cdot \sin(\theta_B) \quad (5).$$

For a polycrystalline material or randomly distributed powder, so called Debye-Scherrer rings (DS-rings) arise as an overlap of the diffracted beams of the individual crystallites as can be seen in Fig. 5. The intensity and the shape of the rings depend on the crystalline structure of the sample. When making a cut through the DS-rings and drawing the intensities over two times the diffraction angle 2θ (radial direction of the DS-rings), a so called diffractogram is obtained. This diffractogram is the result of a typical laboratory XRD measurement from which different properties of the material, such as lattice parameter, crystal orientation and residual stress, can be determined [49].

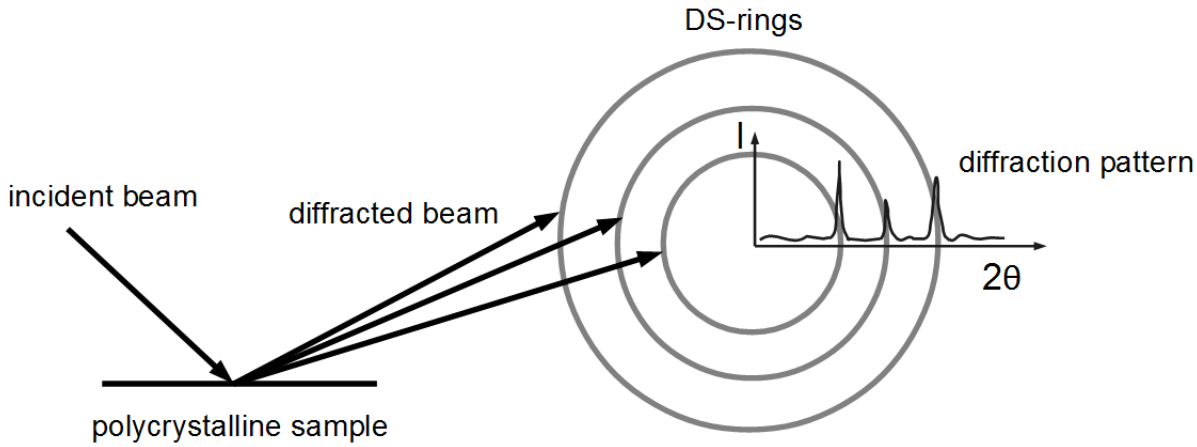

Figure 5: Debye-Scherrer rings created by diffraction on a polycrystalline sample with an exemplary diffractogram at one azimuthal angle of the rings.

The incident X-ray beam, generated by an X-ray tube, consists of characteristic radiation and the continuous Bremsstrahlung. The characteristic radiation results from the collision of accelerated electrons with a target. The collision ionizes the target atoms due to removing

an electron of an inner atom shell. This empty electron site then is occupied by an electron of an outer shell, resulting in the emission of a photon with a wavelength characteristic for the element [50]. The target material frequently is Cu or Mo, but also Cr, Fe or Co can be used. Depending on the target material, the emission profile can exhibit one or more peaks with defined wavelengths surrounded by a less intense Bremsstrahlung-spectrum [49, 51].

For cutting off a part of the unwanted wavelength spectrum, often a filter is used. The filter (e.g. Ni for Cu radiation) absorbs the radiation partly, so that the radiance above or beneath a specific value (absorption edge) is removed or at least strongly reduced in intensity [50]. To confine the beam to one single wavelength, a monochromator can be used. This is a single crystal, only diffracting the wavelength of the beam spectrum which fulfills Bragg's law [50]. The rest of the emitted spectrum is absorbed by, or transmitted through the crystal. These two devices can be placed directly after the X-ray tube and/or before the detector. When an energy dispersive detector is used, an external monochromator is not necessary, as it only measures photons with a certain energy [52]. Further devices in the beam path can be mirrors, either for collimating (e.g. Goebel mirror) or for focusing (e.g. toroidal mirror) the divergent beam onto the sample [51].

Additionally, Soller slits and divergence slits can be used to restrict the divergence of the beam. A Soller slit is a set of fine parallel foils, with defined distances between them, to limit the divergence of the beam in equatorial direction. The divergence slits can be adjusted to different values for limiting the beam width and consequently the divergence in the radial direction. Compared to mirrors, slits have the disadvantage of reducing the intensity of the beam due to shielding parts of it [49, 51]. The next part in the setup is the sample holder, which can be a planar plate or a glass capillary, for instance. This sample holder also can be installed in a heating, cooling, or vacuum chamber to measure at non-ambient conditions. The sample holder is often used to rotate the sample during the measurement to receive averaged results over the sample area. The diffracted beam can pass mirrors and slits after being diffracted at the sample, which have basically the same functions as their counterparts on the incident beam side. Eventually, the beam is recorded by a detector producing a digital signal [51].

In general, the principle of operation of an XRD device can be divided into reflection and transmission geometry, depending on whether the incident beam is passing through the sample (powder in glass capillaries or thin foils) or it is reflected on the sample surface (thick

samples or powder on planar plates) [51]. Figure 6 shows an example of an X-ray diffractometer arrangement in so-called Bragg-Brentano geometry, i.e. in a symmetric reflection geometry with a divergent beam [49].

Three sorts of detectors are available for XRD, classified as point (0D), linear (1D) or area (2D) detectors. Point detectors, which are most common in laboratory X-ray diffractometers must be moved over a 2θ range to determine the diffractogram, whereas the other two can be fixed to a specific 2θ value since they measure a larger 2θ range at once. With a 2D detector, depending on its size, it is possible to measure up to whole DS-rings at once, providing faster collection of the information, as often used in synchrotron devices. Using a 0D or 1D detector, the diffracted beam can only be measured at one azimuthal angle of the DS-rings. [51]

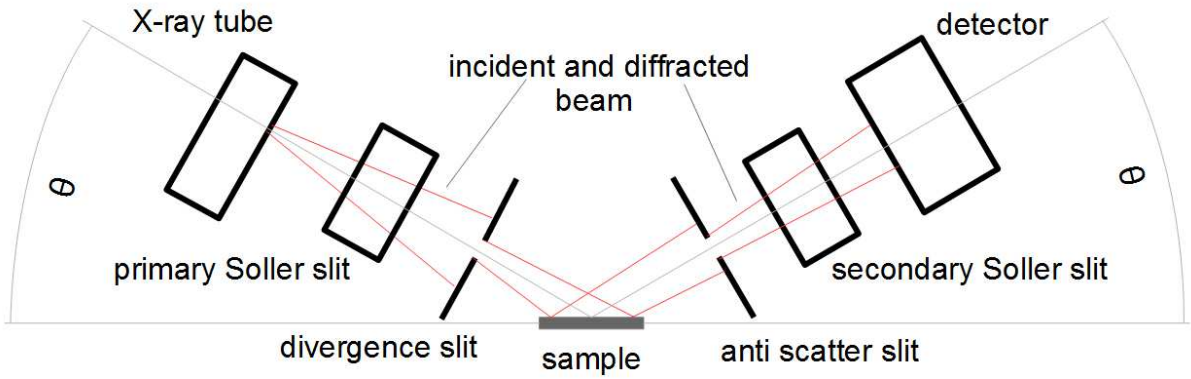

Figure 6: Arrangement of XRD in Bragg-Brentano geometry (reflection geometry and divergent beam).

When measurements are performed at HT, e.g. to measure the thermal expansion of a material, the sample has to be installed in a special HT chamber as mentioned before. Such chambers have to be calibrated before usage because there are always uncertainties in temperature level. These are due to the fact, that the sensor is mounted in a certain distance to the sample. Also the pressure in the chamber and the used gas can affect the measured temperature. For this calibration, three different proceedings are suggested [53–55]:

1. The measurement of the expansion of well characterized materials, like e.g. Pt.
2. The measurement of temperature at polymorphic phase transformations, like the α/β-transformation of SiO_2 for instance, where the transformation can be noticed in a disappearance of peaks and appearance of new ones depending on the new phase.

3. The determination of the melting point of materials, like NaCl or Au. At the melting point, the measured Bragg-reflections disappear.

As written above, the result of an XRD measurement is a diffractrogram from which the following information can be received:

- The observed phase composition and the lattice parameter are calculated from the intensities and the diffraction angle of the peaks [49, 52].
- The crystallite size and the quality of the defect density and microstrains can be estimated from the full width at half maximum (FWHM) [56].
- When measuring the sample at different tilt angles, which means at different orientations of the diffraction angle Ψ, it is also possible to determine the elastic strains and subsequently residual stresses from the Bragg-angle [52, 56].

To receive all this output, the peaks have to be analyzed as precisely as possible. For this analysis, different peak fitting and refinement methods can be found in literature. One of the most popular approaches used for diffractogram evaluation is the Rietveld method [57].

2.3.2 Rietveld refinement

The Rietveld method developed by Hugo Rietveld in 1966 [58] is a refinement method first only used for the analysis of neutron powder diffractograms and later also for X-ray powder diffraction [59]. As the refinement in this work was done by the Rietveld method of X-ray powder diffraction, the following description will only concern XRD data. The innovation of the Rietveld method was to analyze the diffractogram in its entirety, including the background and not only individual peaks. Consequently, it is possible to refine complex structures with overlapping peaks, which would affect the refinement of each other, when only single peaks are taken into account. The mathematical principle behind the technique is a least square method as shown in eq. 6, where the aim is to minimize the parameter *M* by summation over all points in the pattern [57]

$$M = \sum_i w_i \, [y_i - y_{ci}]^2. \tag{6}$$

In this equation w_i is the weighting factor, depending on the variance of the total intensity and the background intensity and it represents the statistical errors of the observed intensities. Mostly it is reduced to

$$w_i = 1/y_i, \tag{7}$$

due to the assumption that the variance of the background is zero. However, this often results in an overestimation of the weighting factor. y_i and y_{ci} are the observed and the calculated intensities at the i^{th} step, respectively, where the observed intensity consists of the total minus the background intensity [57, 59–61].

Simply described, the method creates an approximate model of the diffractogram on the basis of input parameters. This model is then refined by the least square method in iterative steps until the best possible approximation to the measured pattern is found. In other words, until the minimum of the difference between the calculated and the observed intensity is reached. An example of such a measured diffraction peak (points) and the refined model (continuous line) is shown in Fig. 7 for the evaluation of the diffractogram from a KCl sample [62]. The line beneath the peak states the y_{ci}-y_c – difference plot as briefly described later in this chapter.

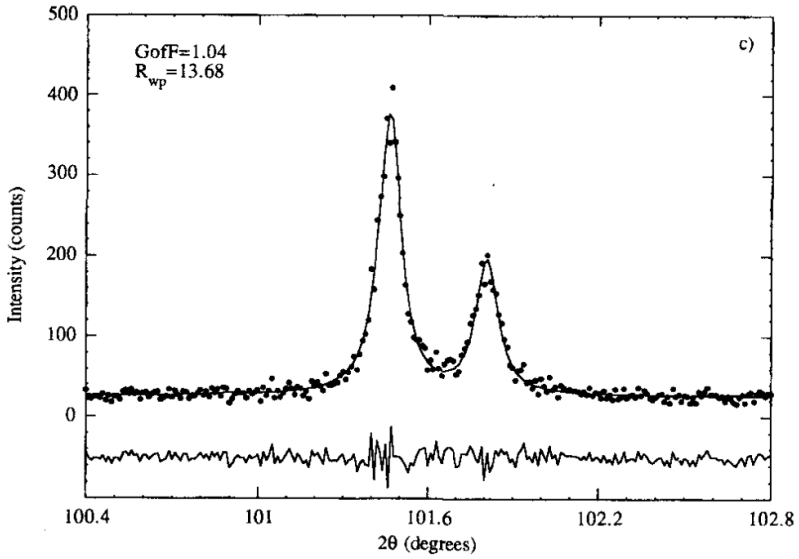

Figure 7: Curve fitted to an XRD measurement of KCl (dots) and y_{ci}-y_c – difference plot [62].

Two different types of practicing the Rietveld method can be found. The first type, nowadays out-of-favor, was developed by Rietveld. It includes mainly two groups of parameters which can be refined in principle simultaneously [59–61]:

- First, the structural parameters like the fractional coordinates of the atoms, the overall temperature parameter, or the scale factor.
- Second, the profile parameters like half width factors, unit-cell values or the zero position of the detector for instance.

Generally, a very important part of the refinement is the profile shape function used to converge the model to the measured data because a precise profile shape description is the key feature of every Rietveld refinement. In the first type, the shape functions which are fitted to the measured data are mostly Gaussian, Lorentzian, Pseudo Voigt and Pearson VII functions. The shape of the peaks determines the used shape function incorporated in y_{ci} [61, 63]. Great efforts have been made in the past to find other functions for better fitting results, like the modified Lorentzian function of Malmros and Thomas and many others [60, 64]. All these functions include the FWHM, which is getting broader at higher diffraction angles θ, as described by Caglioti *et al.* for neutron powder diffraction [65]. It was modified to the simple equation

$$FWHM^2 = V \cdot tan\theta + W \tag{8}$$

for X-ray powder diffraction by Khattak and Cox, where *V* and *W* are variable parameters in the profile refinement [66]. As stated by Will, these equations are only taken for instrumental broadening of the peaks [61].

The second and nowadays commonly used type is the so-called fundamental parameter approach. It includes a third group of parameters named the instrumental parameters, which comprise the slit dimensions, the angle of divergence of the beam or the X-ray source size. In this type, the profile shape functions are not specific like written above, but convolutions of Gaussian, Lorentzian and other simple functions [52]. Furthermore, the instrumental broadening of the peaks is not described by one single equation, like eq. (8), but by the instrumental parameters, which are refined in the method. Depending on the diffractometer configuration (divergent, parallel) and the arrangement, different instrumental parameters have to be taken into account. This instrumental broadening function can be subdivided into the geometric instrument profile and the wavelength profile function as can be seen in Fig. 8. Together with the specimen broadening function, the calculated profile function (convoluted function) is generated [67–70]. The greatest advantages of this technique are that a misalignment or a false setting in the diffractometer can be realized quickly when evaluating the functions. Moreover, the fitted 2θ peak positions are automatically corrected for nearly all instrumental aberrations [67].

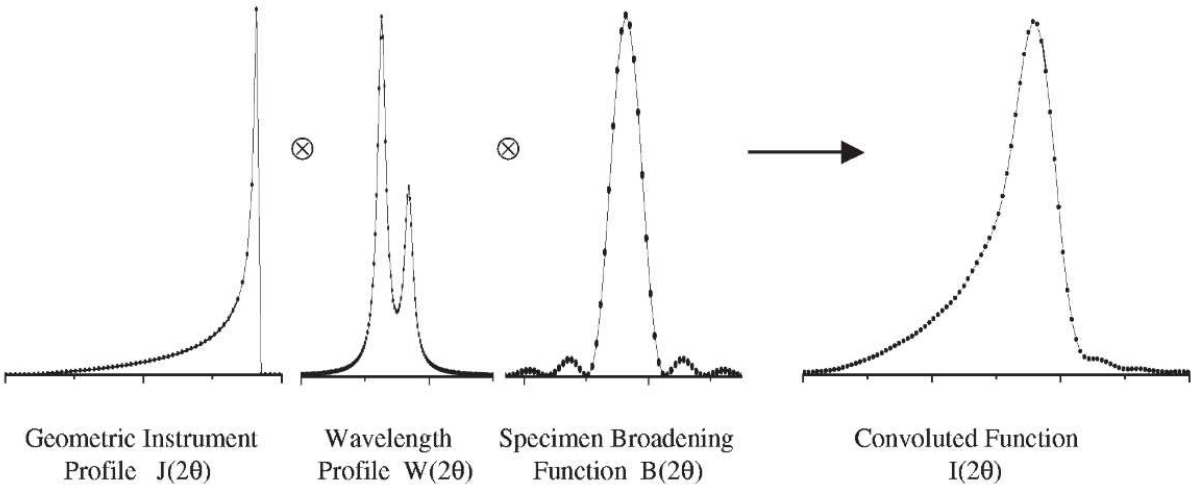

Figure 8: Contributions to the overall profile function $I_{(2\theta)}$ consisting of the instrumental broadening function (convolution of geometric instrument profile $J_{(2\theta)}$ and wavelength profile $W_{(2\theta)}$) and the specimen broadening function $B_{(2\theta)}$ [68].

As the method is not a structure solving, but a structure refinement method, it is important to feed it with best possible starting parameters including values of all refineable parameters, wavelength data, and 2θ limits. Otherwise it can easily run into a false minimum, resulting in wrong output. The number of parameters which can be included in the refinement depends on the resolution of the diffractogram [59].

After refining a powder diffractogram it is essential to check if the fit and consequently the results are plausible. Different criteria of fit are suggested in literature, like y_{ci}-y_c – difference plots, the maximum deviation of the calculated and the measured intensity, the goodness of fit *GOF* or different so called R-values [61]. y_{ci}-y_c – difference plots are taken for visual analysis of the quality of the fit as can be seen in Fig. 7. This should in the best possible case be a straight horizontal line. Mostly used R-values are the Bragg R-value or the (weighted) profile R-value R_B or R_{wp}, respectively. R_{wp} can be calculated using

$$R_{wp}^2 = \sum_i w_i [y_i - y_{ci}]^2 \Big/ \sum_i w_i [y_i]^2 \quad [71]. \tag{9}$$

Reasonably, the best possible R_{wp}-factor is the so called expected R-factor R_{exp}, which is obtained when the term $w_i(y_{ci} - y_i)^2$ is set equal to one [71]. *GOF* than can be determined as the ratio of R_{wp} and R_{exp}. When calculating these R-values, one has to be cautious which equation is used and whether the background is removed at first or not [61, 71]. Jansen

stated, that a high background greatly affects the *R*-values, which consequently appears better, i.e. the *R*-values seem smaller as they are [72].

To account for the background, there are often parameters set to refine the background as well in modern Rietveld programs. However, there are still some problems when refining materials with amorphous contributions. In general, it can be said that a lower *R* or *GOF* value indicates a better fitting result. But it is of high importance that *GOF* should not be below one or in other words R_{wp} should not be smaller than R_{exp}. If this is the case, either the standard uncertainty of the data has been overestimated or too many parameters have been introduced and so the method might be fitting essentially noise. This could be also the case if the values are close to one or R_{exp}, respectively [71].

It should be noted, that no clear threshold value for any *R* or *GOF* indicating a good fit can be defined. First, however, not just the fit of the structural model is rated, but also the fit of the background, the diffraction positions and the peak shapes. Second, the quality of the diffractogram is of high importance because when counting longer even minor imperfections in the peak have influence on *R* and *GOF* [71].

3 Experimental methods

3.1 Production of Ti(C,N) powder

The materials for this thesis were synthesized by nonreactive, unbalanced magnetron sputter deposition with the laboratory deposition device “Josefine II” at the Department of Physical Metallurgy and Materials Testing at the Montanuniversität Leoben. An illustration of the device is shown in Fig. 9. It consisted of a cylindrical steel vacuum chamber with an inner diameter of 305 mm and a height of 410 mm. Three magnetrons were installed in the chamber in a triangular arrangement, which could be adjusted in orientation to show towards the substrate. On each magnetron a target was mounted, which could be covered by a movable shutter. The used planar, circular targets were TiC and TiN from FHR centrotherm group with a diameter of 51 mm and a thickness of 6.4 mm. The purity of the targets was 99.5 %. The generation of the vacuum was done by two vacuum pumps, a dual stage rotary vane pre-pump (Pfeiffer duo 20) and a turbomolecular pump (Pfeiffer TMH 521 P). For measuring the vacuum, a DCU display unit and a PKR 251 Compact Full Range pressure gauge from Pfeiffer Vacuum were used. The power supply for the magnetrons, as well as for the etching potential, was provided by three ENI MKS RPG-50 generators, which could be regulated on constant voltage (used for the etching potential) as well as on constant current (used for the magnetrons) mode. With a heating unit AJA Int. SHQ-15A, working with two halogen bulbs with a power of 1 kW each, mounted on the backside of the substrate holder, the temperature of the substrate was adjusted.

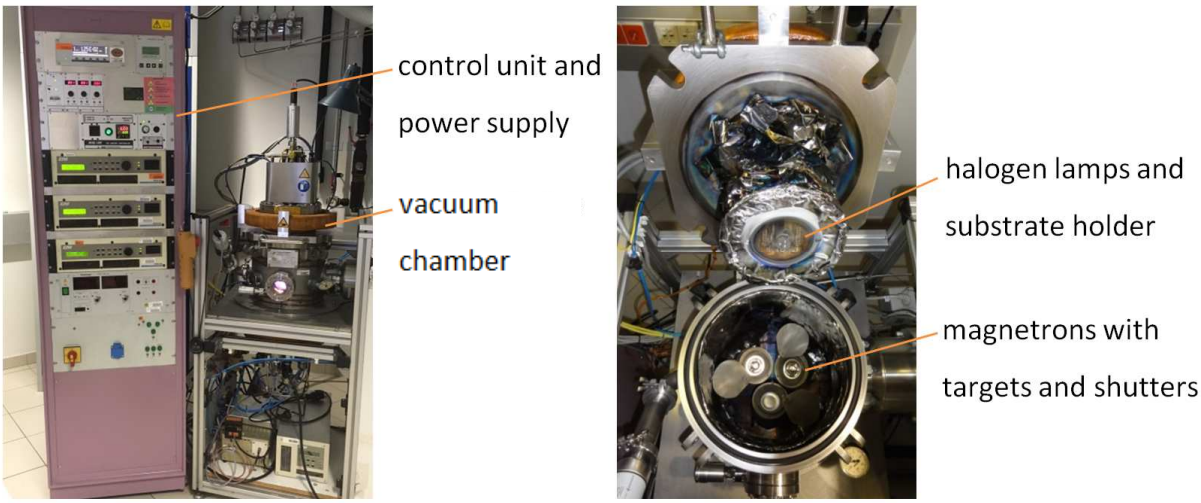

Figure 9: Magnetron sputter deposition plant “Josefine II”

The used substrate for the different deposition runs was a circular mild steel foil with a diameter of about 9 cm and a thickness of 0.05 mm. After cleaning the foil with acetone and ethanol in an ultrasonic bath, it was mounted on a rotating substrate holder in a distance of 75 mm to the targets.

Before starting the deposition, the vacuum chamber was pumped down to a pressure of less than $1 \cdot 10^{-5}$ mbar. Then the substrate was cleaned by plasma etching and the targets by sputtering for a duration of 10 min. Ar with a flow rate of 200 sccm was used as process gas for the cleaning step. The substrate etching potential was set to -500 V and the target current to 0.1 A. During the cleaning cycle, the shutters in front of the targets were closed. For the deposition, the Ar flow rate was regulated to a value of 30 sccm. The resulting working pressure in the chamber was about $5.3 \cdot 10^{-3}$ mbar. To obtain the desired alloying contents of the Ti(C,N) coatings, the target currents were set to the values presented in Table 1. The coatings are varying from TiN to TiC in equal steps of 10 at.-% of the nonmetal. For deposition, the temperature of the substrate was held constant at 500 °C and no bias voltage was applied.

Table 1: Target currents used for the TiC (I_{TiC}) and TiN (I_{TiN}) targets for different Ti(C,N) depositions

Coating	I_{TiC} [A]	I_{TiN} [A]
TiC	0.4	0
$TiC_{0.9}N_{0.1}$	0.36	0.02
$TiC_{0.8}N_{0.2}$	0.32	0.04
$TiC_{0.7}N_{0.3}$	0.28	0.06
$TiC_{0.6}N_{0.4}$	0.24	0.08
$TiC_{0.5}N_{0.5}$	0.08	0.16
$TiC_{0.4}N_{0.6}$	0.16	0.12
$TiC_{0.3}N_{0.7}$	0.12	0.14
$TiC_{0.2}N_{0.8}$	0.08	0.16
$TiC_{0.1}N_{0.9}$	0.04	0.18
TiN	0	0.4

The duration of every deposition run was 4 hours to achieve a layer thickness of about 1 µm. After deposition, the coated steel foils were dissolved in an aqueous solution of 20 vol.- % HNO_3 at 70 °C for about one hour. During dissolving, the Ti(C,N) layer broke into small flakes, which were washed with water and acetone. Afterwards they were filtered and dried, before pulverizing them with a mortar.

3.2 XRD measurements

3.2.1 X-ray diffractometer

The XRD analysis of the powders was performed on a Bruker D8 Advance X-ray diffractometer. A sketch of the arrangement can be seen in Fig. 10 a) and a picture of the diffractometer in Fig. 10 b). For the production of the beam, an X-ray tube Siemens KFL Cu 2KDC working with a Cu anode was used. The values for the tube current and voltage were set to 40 kV and 40 mA, respectively. The divergence in equatorial direction was restricted by a variable divergence slit set to 0.1° and the divergence in radial direction by a Soller slit with an angle restriction to 2.5°. As sample holders, quartz glass capillaries with an outer diameter of 0.5 mm, a wall thickness of 0.01 mm and a length of 80 mm were used, which were rotated about the longitudinal axis during the measurement. These glass capillaries were placed in a capillary attachment mounted to an Anton Paar HTK 1200N heating chamber. Next to the sample, on the secondary side, an anti-scatter slit, with an opening angle of 4°, and an analogous 2.5° Soller slit as on the primary side were placed. For measuring the diffracted beam, a position sensitive, energy dispersive 1D Lynxeye XE-T detector was used. The measurement was carried out in Debye-Scherrer geometry with a fixed X-ray tube at 0° [52].

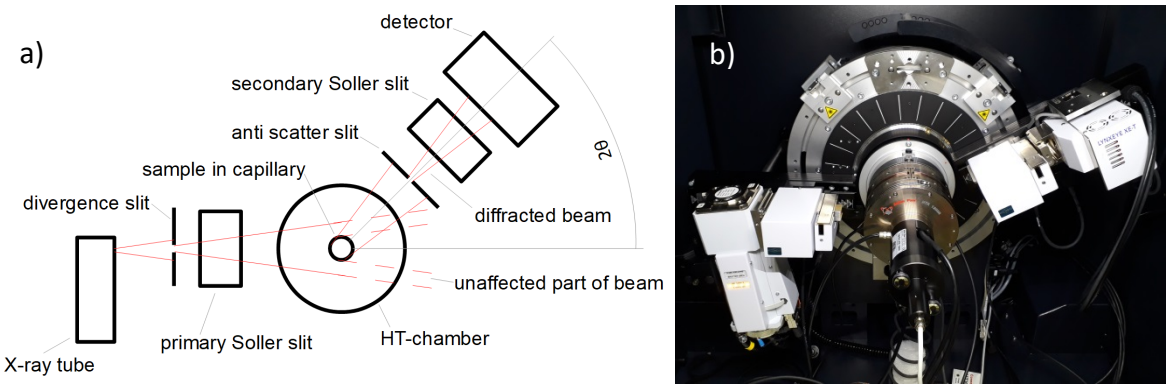

Figure 10: Sketch a) and picture b) of the X-ray diffractometer arrangement.

For the measurements, the capillary had to be aligned with respect to the X-ray beam. This was done by measuring the direct beam with the detector ($2\theta = 0°$) for 10 s. As the direct beam is of much higher intensity than the diffracted beam, the voltage and the current had to be lowered to 20 kV and 5 mA, respectively, in order to not harm the detector. Also a 0.1 mm thick Cu absorber was put into the secondary beam path to diminish the intensity. The positioning of the capillary then was executed by varying the height of the HT chamber until the lowest intensity of the detected beam was at $2\theta = 0°$ with a symmetric intensity profile on either side, as can be seen in Fig. 11. The decrease of the intensity in the middle is caused by absorption of the filled capillary. To obtain the thermal expansion for the different coating compositions, the powders were then measured at temperatures varying from 25 to 1000 °C in steps of 50 °C.

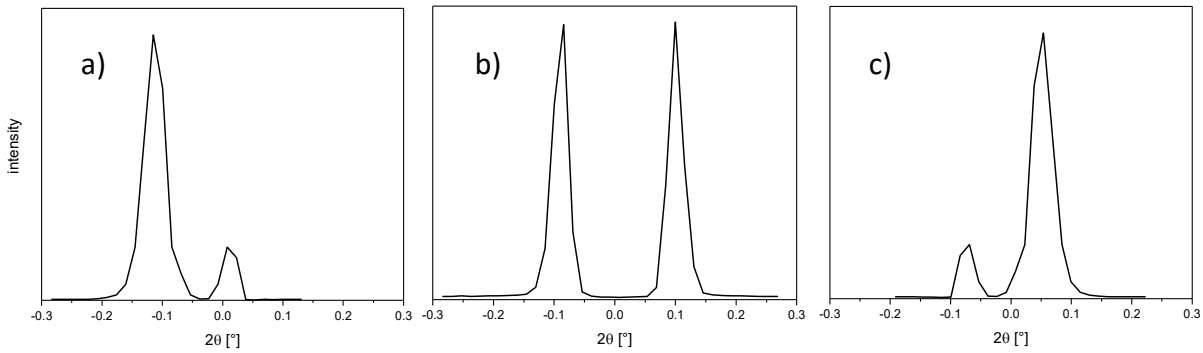

Figure 11: Intensity distribution for a) a too high capillary, b) a well aligned capillary and c) a too low capillary.

3.2.2 Calibration of the HT chamber

In order to adapt the set sample temperature, the system was calibrated before executing further measurements. The characterization of the arrangement at room temperature was done by the measurement of standard LaB_6 powder "NIST 660c" [73] in a 2θ range from 20 to 85°. The powder was measured with a step size of 0.01° and duration of 0.4 seconds per step. Subsequently, the HT calibration was carried out with three different methods in the range of 25 to 1000 °C.

- The first method was the measurement of the thermal expansion of a standard Pt powder in temperature steps of 25 °C and a 2θ range of 35 to 85°. The counting time was 0.4 seconds per step and the step size 0.01°. The used powder, provided by Goodfellow Cambridge Limited, had a purity of 99.95 % and a particle size of 3.5 µm.

Before measuring the lattice expansion, the Pt powder was recrystallized at 1000 °C for 10 min to avoid microstructural changes during the measurement. The delay time between every temperature step was 5 min to guarantee isothermal conditions during the measurement. For a better statistical evaluation, the diffractograms were recorded twice, during a heating as well as during a cooling ramp. The lattice parameters for every step were compared to thermal expansion literature data [74, 75]. Due to the comparison of the measured and the literature lattice constants, a difference in temperature and thereof a calibration curve could be calculated.

- Second, an Omega SCAIN-IM025E-150-SHX type K thermocouple with a diameter of 0.25 mm and a length of 150 mm was inserted into the capillary, so that the temperature inside the capillary could be directly measured over the whole range. The measured data of the thermocouple was converted and displayed by a Jumo cTRON 08. With this data also a calibration curve could be obtained.
- To confirm the calibration curves at different points, the third method was the measurement of the solid/liquid phase transition of Sn, Zn and Al powder.

3.2.3 Measurement of the Ti(C,N) samples

After calibrating the HT chamber, the different Ti(C,N) powders were measured between 25 and 1000 °C with steps of ΔT = 50 °C in the 2θ range of 35 to 79°. The counting time was set to 0.4 seconds per step and the step size to 0.01°. To shorten the measurement time, the 2θ ranges between the peaks were recorded with an increased step size of 0.25°. The different 2θ ranges as well as the corresponding step sizes are shown in Table 2. As the powders synthesized by magnetron sputter deposition usually contain a significant amount of defects, they were annealed for 15 min at 1000 °C in order to recrystallize them before measuring the lattice parameters [76].

Table 2: 2θ ranges for different step sizes

$2\theta_{Start}$ [°]	$2\theta_{End}$ [°]	step size [°]
35	38	0.01
38	40.5	0.25
40.5	43.5	0.01
43.5	59.5	0.25
59.5	62.5	0.01
62.5	71	0.25
71	79	0.01

3.2.4 Lattice parameter refinement

The analysis of the measured X-ray data was performed by the refinement of the lattice parameter, based on the space group of Ti(C,N) using the program Topas V6. The aim of the refinement was to obtain the lattice parameters at each temperature step to calculate the TEC. The model was refined by the use of the fundamental parameter approach. As emission profile the CuKa_5-Berger data file, provided by Topas, was used. The background was fitted by a 1/X-function and a Chebyshev polynomial function of the 5th order. For the fit of the diffractogram, an hkl_phase was used, where the input for the existing peaks was given by the space group number, which is 225 for Ti(C,N).

In addition to the background, the following parameters were refined in Topas:

- zero point error
- crystallite size
- strain
- lattice constant *a*.

For the refinement of *a,* an initial input value close to the real one had to be set. The values were 3.9 Å for Pt, 4.3 Å for TiCN and 4.2 Å for LaB_6.

4 Results and discussion

4.1 Calibration of the X-ray diffractometer

4.1.1 Room temperature verification of XRD setting

In order to verify the measurement precision of the used X-ray diffractometer, the lattice parameter of a LaB_6 powder standard (NIST 660c) was measured at room temperature. The result of this experiment can be seen in Fig. 12, where the measured lattice constant of the LaB_6 is compared to the value of the certificate supplied by the National Institute of Standards and Technology (NIST) [73]. The measured and certified values of the lattice parameters are 4.156861 ± 0.000043 Å and 4.156826 ± 0.00008 Å, respectively. The difference of 0.000035 Å most probably results from the fact, that the measurement was performed at 25 °C, but the accredited value is valid for 22.5 °C. Taking this temperature difference into account, an increased value of the lattice parameter is expected, which is in good correlation with the measurement. When taking the error of the certified value into consideration, the measurement gives a good verification of the used setting at room temperature.

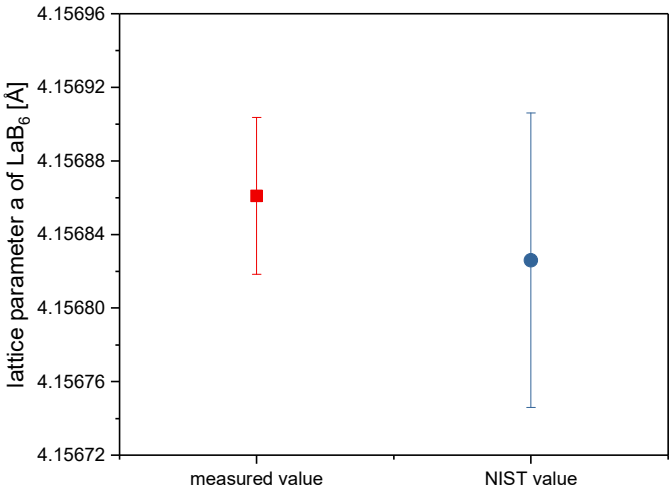

Figure 12: Lattice parameter comparison of NIST 660c-standard LaB_6 powder: ■ value measured using the XRD, where the error bars illustrate the estimated standard deviation calculated by the software Topas V6; ● value and deviation from the NIST certificate [73].

4.1.2 High temperature calibration

For the temperature calibration of the high temperature chamber, three different methods were applied.

Calibration using Pt powder

The first method was the determination of the temperature dependent lattice parameters of a Pt powder. The complete recorded diffractograms for 25, 500 and 1000 °C of one Pt measurement are drawn in Fig. 13 a). In Fig. 13 b) the region of the peaks at the highest diffraction angles in the diffractogram is enlarged. This provides a clear look on the peak shifting to smaller diffraction angles with increasing temperature due to thermal expansion. As can be seen in Fig. 13 b), one peak is divided into two subpeaks as a result of the diffraction by the Cu-Kα_1 (left) and the Cu-Kα_2 (right) radiation.

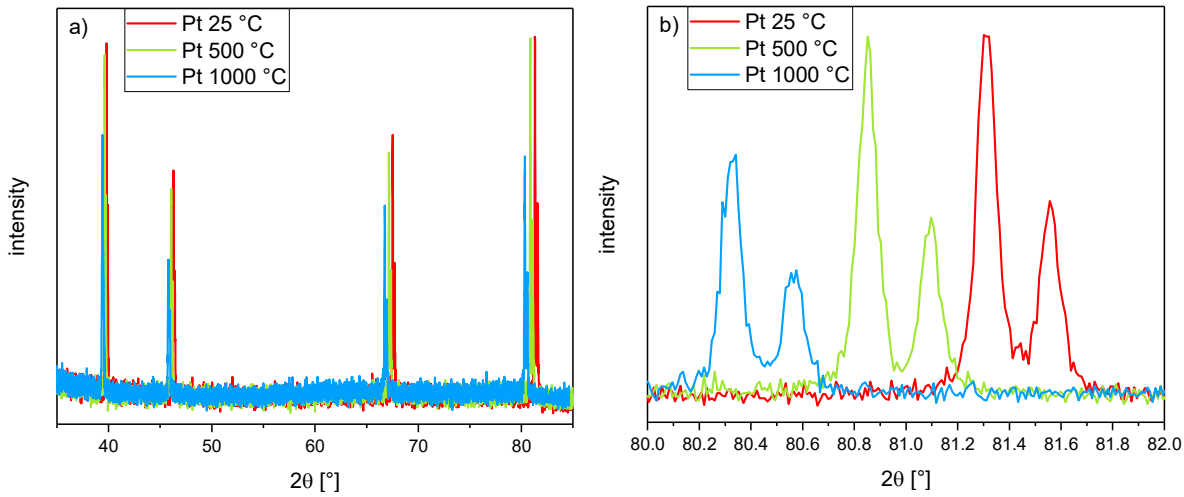

Figure 13: a) Diffractograms of Pt measurements at 25, 500 and 1000 °C over the complete measured 2θ range of 35-85° and b) peaks at the highest measured diffraction angles enlarged for better comparison.

From the recorded diffractograms, the lattice parameters at different temperatures were calculated and plotted over the temperature as can be seen in Fig. 14 a). In this graph, the lattice parameters of one Pt measurement are compared to the function of the temperature dependent lattice parameter of Pt determined by Arblaster [74]. Thereof, the difference between the set and the present temperature can be calculated, as exemplarily shown in Fig. 14 b). At a set temperature, like e.g. 725 °C, the measured lattice parameter is 3.9516 Å.

This lattice parameter should however be present at a temperature of 742 °C according to [74]. Thus, the actual temperature of the sample is 742 °C in this case, which results in a temperature difference *ΔT* between the real and the set value of 17 °C. The set temperature has therefore to be corrected for further evaluations by adding the temperature dependent *ΔT*.

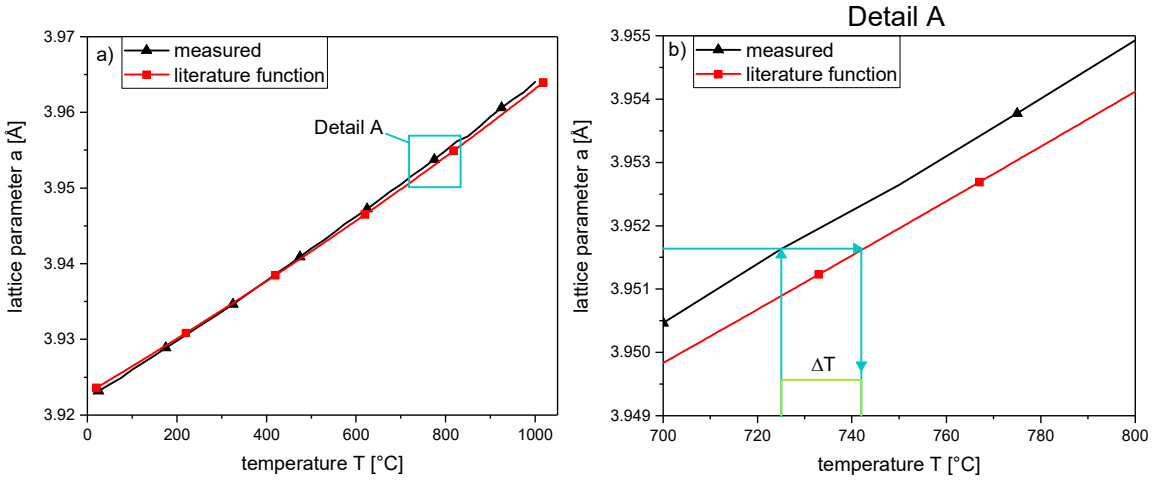

Figure 14: a) Comparison of the measured lattice parameters of one Pt measurement with literature data over the temperature range of 25-1000 °C. b) Graphical depiction of *ΔT* calculation.

The results of one measurement cycle are exemplarily shown in Fig. 15 over the complete temperature range from 25 to 1000 °C. The data is separated into the measured heating ramp “up”, from 25 to 1000 °C and the cooling ramp “down”, from 1000 to 25 °C. The average curve shows the averaged values of the up and down ramps. Five different Pt measurements were conducted and evaluated using this method to guarantee a statistical validity of the Pt calibration. Two of these measurements were conducted using the same capillary, whereas for the other three, different capillaries were used. Between the measurements, also the HT chamber was exchanged to a Eulerian cradle and the opening angle of the slits was varied several times to verify the reproducibility.

All the Pt measurements exhibit the same trend of a rising *ΔT* with increasing temperature in the HT chamber up to a set value of approximately 800 °C. Then the *ΔT* stays nearly constant or is even decreasing. The green curve (▼) represents the average *ΔT,* where a different start value of *a* at 22.5 °C for the lattice parameter function was used [74]. While for calculating the brown curve (■), the measured value at 25 °C extrapolated to 22.5 °C by the

mentioned lattice parameter function in [74] was taken as starting point, for calculating the green curve the literature value of Arblaster for 22.5 °C [75] was taken as starting point. Hence, the difference between the red and the green average curves indicates the difference in lattice parameters between the measured sample and the sample used in ref. [75], including a possible temperature independent error. At 25 °C the highest difference of the lattice parameter is approximately 0.0006 Å for the various samples measured. This deviation is, however, about ten times higher than the observed one for the LaB_6 measurement. The differences in ΔT at 25 °C between the two averaged curves (literature start and recorded start) of the other four Pt measurements were varying in the range of the one drawn in Fig. 15 and zero. The displayed average curve with the measured starting value also exhibits the highest ΔT. Thus, all other recorded Pt curves lie between the two displayed average curves in Fig. 15.

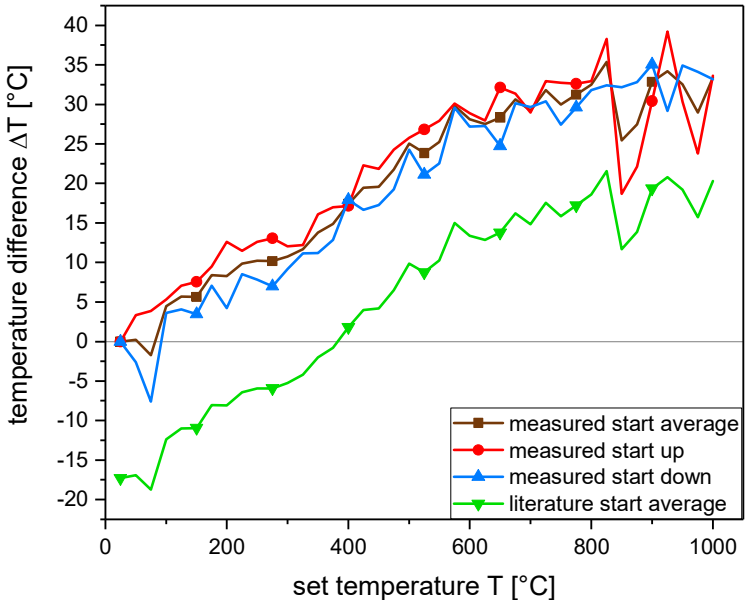

Figure 15: Temperature difference to literature data [74] of Pt measurement in the temperature range of 25 to 1000 °C, with the start value calculated by the measured lattice parameter (■) and the start value from [75] (▼).

The difference in temperature from the measured values to the values calculated by the literature function has several reasons. First, the HT chamber can be used to measure bulk samples lying on a sample holder as well as for powders in capillaries. The thermocouple in the chamber is located underneath the sample position for bulk samples and is also calibrated to this place [77]. Thus, there is a significant distance between the inserted

capillary and the thermocouple and therefore the capillary and the sensor are not thermally connected to each other. For that reason, the chamber is not precisely calibrated for a capillary measurement and due to differences in thermal irradiation such a temperature deviation can occur. Also the presence of the anti-scatter slit in front of the capillary, and the thermal properties of the sample influence the temperature deviation [78]. Another possible reason for the variation of the lattice parameters for the different Pt measurements is, that the Pt powder in the capillaries sinters together when first heated to 1000 °C. During the sintering process, the volume of the powder in the beam changes and thus, the Pt does not fill the whole capillary and might not be perfectly aligned in the center of the capillary anymore. However, this should only have a minor influence on the results, since the capillaries were rotated during the measurement compensating for possible misaglinment. Also the glass capillaries may to some extent be responsible for the varying lattice parameter as they partly exhibited small differences in diameter because of manufacturing tolerances. The thermal expansion of the samples and the capillaries can be another influencing factor on the diffractrogram. Especially if the capillary shows unisotropic thermal expansion, the sample may be shifted out of the beam center.

In general, the heating and cooling curves in Fig. 15 are very close to each other, with only a slightly lower ΔT for the average cooling ramp and some outliers at elevated temperatures. To verify the difference as insignificant, the average curves of the five heating and cooling cycles are drawn in Fig. 16. In the lower temperature range up to about 650 °C, the ΔT and thus the lattice constant of the cooling cycle exhibits smaller values, than the one of the heating cycle. At higher temperatures this trend diminishes or even turns into the opposite direction. When including the error bars, which represent the standard deviations of the averaged five measurements, these differences in ΔT seem to be completely in the tolerance and thus differences between heating and cooling have not been considered in the consecutive evaluation of the Ti(C,N) .

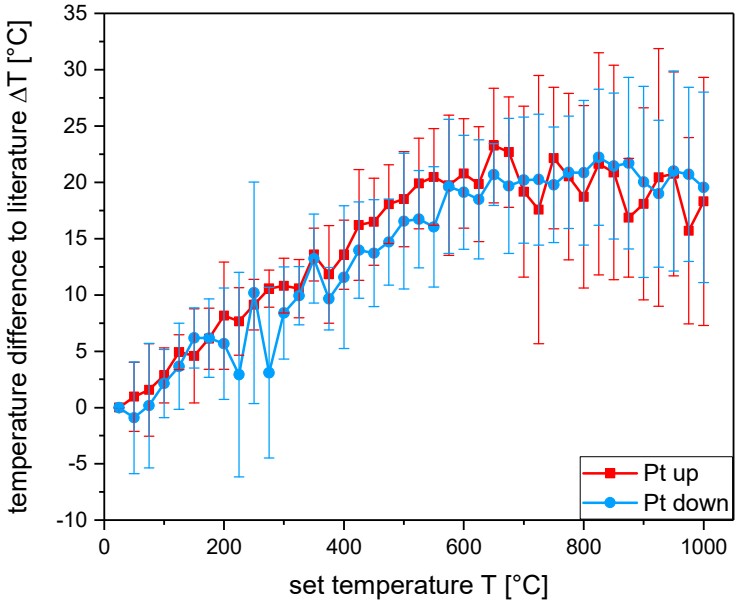

Figure 16: Average curves determined by the five different Pt heating (up) and cooling (down) ramps with error bars, representing the standard deviation of the different measurements.

Taking the above mentioned results into consideration, the average Pt curve, used for the HT calibration, was constructed by averaging all ten different measurement cycles, as can be seen in Fig. 17. This curve then was fitted by a polynomial function of the fourth order (eq. 10), serving as calibration function for further capillary measurements. The fit resulted in the following equation

$$\Delta T = -0.372 + 0.0196 \cdot T + 8.518 \cdot 10^{-5} \cdot T^2 - 1.368 \cdot 10^{-7} \cdot T^3 + 5.074 \cdot 10^{-11} \cdot T^4 , \quad (10)$$

where T is the temperature in °C and ΔT the temperature difference from the real temperature in the capillary to the set temperature at the diffractometer. Equation 10 is valid in the range of 25 to 1000 °C. The ΔT fit increases up to the temperature of 775 °C from 0 to about 20 °C and than it is decreasing again to about 18 °C.

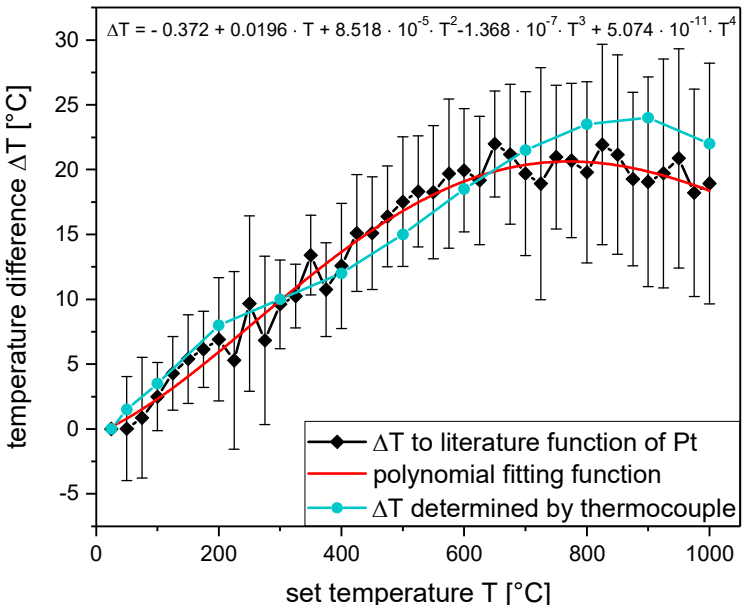

Figure 17: *ΔT* of average Pt curves fitted by a polynomial function of the fourth order compared to the *ΔT* determined by the thermocouple measurements.

Calibration using a thermocouple

To verify the calibration curve determined using the thermal expansion of Pt, the second method was the temperature measurement by a thermocouple directly inserted into a capillary. By subtracting the set values from the recorded values, also a *ΔT* curve as a function of the temperature could be calculated which was averaged by the values of one heating and cooling cycle. This is drawn as comparison to the Pt data in Fig. 17. As can be seen, the curves exhibit the same trend of a rising *ΔT* up to a certain temperature and then they show a decrease.

The differences between the Pt and the thermocouple curves most probably arise as a result of the following two reasons: First and also most important is the position of the measuring tip in the capillary. Even a shift of only a few millimeters out of the beam center resulted in a temperature difference of up to 50 °C. Second, the alignment of the capillary has significant influence on the recorded temperature. As it cannot be rotated during the measurement, differences in thermal radiation cannot be compensated for. Nevertheless, the results of the thermocouple measurement can clearly confirm the Pt calibration curve, when aligned as best as possible in the heating chamber.

Calibration by the determination of melting points

The third HT calibration method was the evaluation of the melting points of three different metals (Zn, Sn and Al) during melting as well as during solidifcation inside a capillary. This was done by heating the metal powders in steps of 1 °C and measuring one selected peak with high intensity at every temperature. The melting point then was identified by the disappearing of the recorded peak. The reverse procedure was done by cooling the liquid metal in steps of 1 °C until the peak was appearing again. With these recorded temperatures, the differences to the melting points from literature ($T_{m(Zn)}$ = 419.53 °C, $T_{m(Sn)}$ = 231.93 °C [79]) of Zn and Sn could be calculated. These are drawn in Fig. 18 compared to the fit of the averaged Pt curve of Fig. 17. It can be seen, that the ΔT calculated for all of the measured melting points are positioned above the Pt curve. This indicates a higher temperature in the HT chamber than determined by the Pt and thermocouple measurements. For Zn, the ΔT recorded during the melting (heating) of the metals exhibits a higher value and hence, indicates a lower melting point, than the one measured during the solidification (cooling). This difference cannot be assigned to overheating or undercooling effects which would show the contrary trend. Since it is smaller than the error bars of the Pt measurement in Fig. 17, the difference between the melting and solidification points of Zn may arise due to inaccuracy of the diffractometer. The difference in ΔT to the Pt curve could otherwise also arise because of a contamination of the Zn with impurities, like for example Al [80], possibly leading to low melting eutectics. However, as the purity of the Zn powder was 99 % such a high deviation in the melting point cannot occur and therefore some unknown error may also influence the results.

The opposite trend, however, can be observed for the Sn measurement, where the temperature measured during solidification lies at a much lower value than measured during melting, which results in a higher ΔT during solidification. This rather high difference in T_m to the literature value may possibly occur because of undercooling effects of the liquid metal [81]. However, as such big temperature differences normally arise at higher cooling rates than applied in this work, an effect, like the β-γ transition of Sn [82], or some other error may also have influence on the measurement.

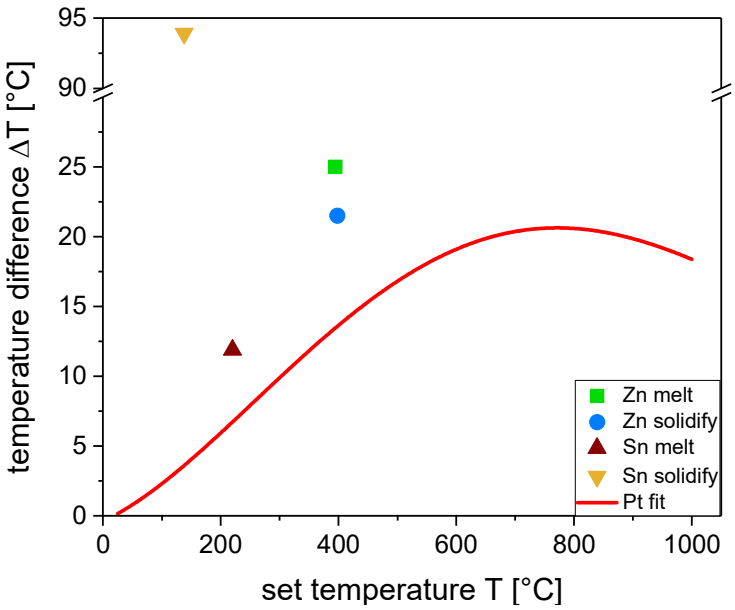

Figure 18: Melting points of Zn and Sn powder determined during melting and during solidification compared to Pt fitting curve calculated by eq. 10.

The measurement of the melting point of Al failed, because the capillary broke during the heating cycle. This could be a result of the chemical reaction of Al with SiO_2, forming Al_2O_3 and Si [83]. Looking at the considerably varying results, the calibration by the determination of different melting points did not result in applicable information due to the above mentioned reasons. Thus, it will not be included in the calibration of the HT chamber. Similarly, a non-successful melting point calibration of a diffractometer in Bragg-Brentano geometry was found by Kern [55].

In conclusion, it can be summarized, that the calibration of the HT capillary setting in the diffractometer results in quite different temperatures compared to the set values. However, the differences are not exceeding 30 °C. This is a typically observed temperature difference as also found by Kern [55] for several different HT XRD chambers. Finally, the calibration curve used for correcting the set temperatures is eq. 10, as it provides high statistical reliability and was in reasonable agreement with the direct temperature measurement with the thermocouple.

4.2 Lattice parameter and thermal expansion of Ti(C,N)

Lattice parameter determination of Ti(C,N)

After calibrating the HT chamber, the measurement of the Ti(C,N) powder was executed in the complete temperature range from 25 to 1000 °C in steps of 50 °C. The recorded Ti(C,N) diffractograms then were fitted using models based on the space group of Ti(C,N), which were refined without taking the first peak at around 36° into consideration. Such a diffractogram including the refined model can be seen in Fig. 19 for TiN at room temperature. The peak at the smallest diffraction angle is excluded to eliminate, or at least to lower the influence of a possibly appearing TiO_2 peak, as it will be shown and discussed later in this chapter. The first appearing TiO_2 peak in the probed range of the diffraction angle would potentially influence the first recorded peaks of the Ti(C,N) samples. This could falsify the determined lattice parameter and consequently the TEC.

To minimize the duration of the measurements, the samples were measured with increased step size between the peaks. This is reflected by an apparently less dense background between the peaks in Fig. 19. The ranges with small step size were optimized, as with increasing temperature the reflection shifts to smaller angles according to Bragg's law [48]. Thus, the peaks in Fig. 19, which were measured at 25 °C, are positioned rightmost in the field of small step size.

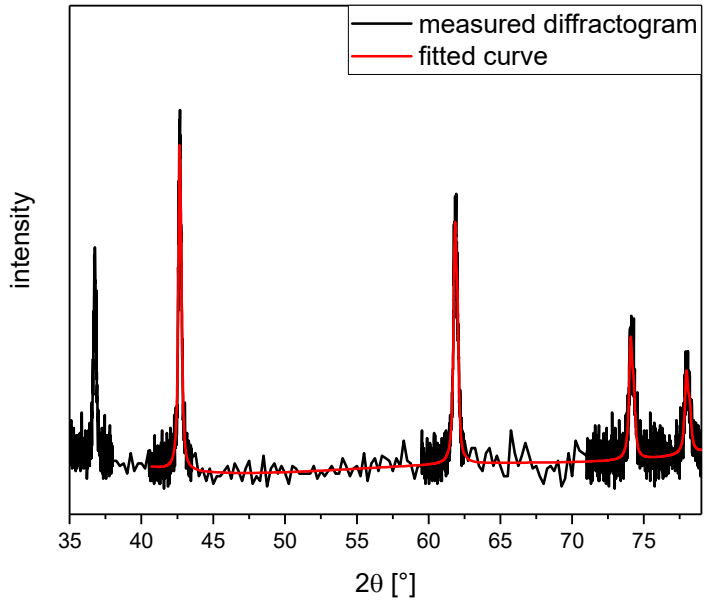

Figure 19: Diffractogram of TiN at 25 °C showing the recorded peaks and the refined fitting curve to the last four peaks.

Together with the knowledge of the actual sample temperature, the fitted lattice parameters were drawn, as exemplarily shown for TiN and $TiC_{0.5}N_{0.5}$ in Figs. 20 a) and b), respectively. Each of these two graphs shows the measured lattice parameter during the heating and the cooling cycle. The fitting errors (error bars in y-direction) calculated by the software Topas V6 represent the estimated standard deviation [55]. These are negligibly small for TiN and thus, almost hidden by the symbols in the graph. For $TiC_{0.5}N_{0.5}$ the fitting errors, as well as the difference between the heating and cooling cycles are somewhat larger. The temperature errors determined by the Pt calibration (see Fig. 17) are displayed by the red error bars in x-direction in Fig. 20. As they are the same for every measurement cycle, they are placed between the two curves. It can be seen, that these error bars exhibit also approximately the size of the symbols and thus, the influence of the temperature error in the chamber is negligibly small after calibration.

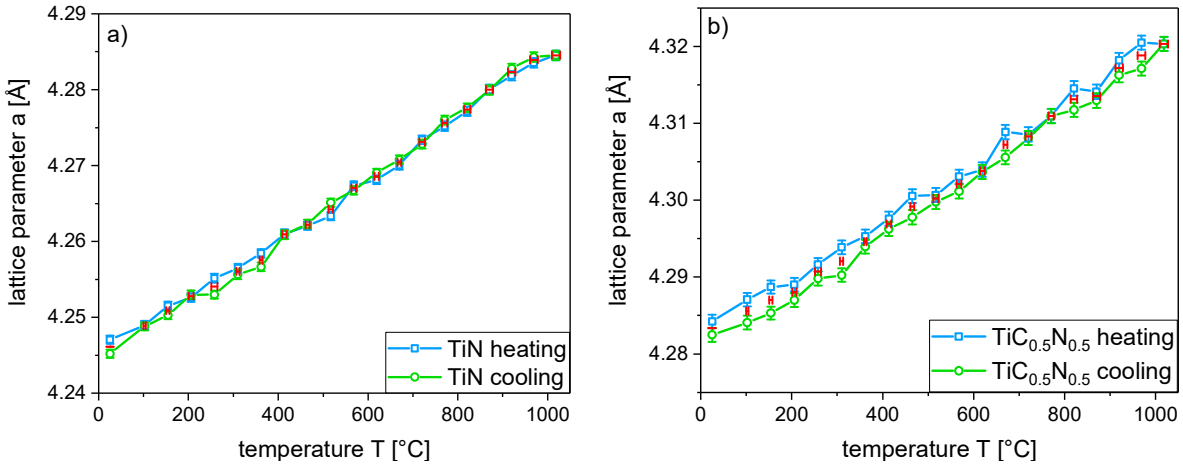

Figure 20: Lattice parameter measured during heating and cooling for a) TiN and b) $TiC_{0.5}N_{0.5}$. The error in y-direction represents the estimated standard deviation of the fits and the error in x-direction represents the temperature error determined by the Pt calibration.

The error of the measurements cannot be described by one simple value, for two different reasons. First, the estimated standard deviation determined by Topas exhibits much smaller values than the difference between the up and down curves and second, each measurement was only carried out once. Thus, there are too few values for a meaningful standard deviation and the error can only be indicated by differences of the heating and cooling curves. The reason for the different heating and cooling values may have a chemical origin

like for instance oxidation during the measurement of the Ti(C,N), which can be recognized by the appearance of TiO_2 peaks in the diffractogram. According to refs. [46] and [47], oxidation should occur at temperatures exceeding 300 to 600 °C. As this effect, except for $TiC_{0.4}N_{0.6}$ which will be illustrated in Fig. 21, did either not or only negligibly arise in the different diffractograms, it does not have considerable impact on the evaluation of the thermal expansion. Another effect, which could influence the lattice parameter, is additional recrystallization as the powder is held at high temperatures much longer during the measurement than during the first recrystallization annealing step at 1000 °C.

The diffractogram of the mentioned $TiC_{0.4}N_{0.6}$ shows no obvious signs of an already present TiO_2 in the capillary after the recrystallization step, as can be seen in Fig. 21 a). Figure 21 b) shows a strong increase in intensity of the TiO_2 (rutile) peaks after the complete measurement cycle. Hence, in contrast to the other compositions, oxidation occurred despite sealing the capillary with glass wool and closing it with the sample holder. Although these TiO_2 peaks were not fitted because only the Ti(C,N) space group was used as input parameter for the refinement, the fit of the Ti(C,N) peaks is most likely distorted by the presence of the TiO_2. Another uncertainty of the measurement is the influence of TiO_2 on the thermal expansion of the sample. Due to these observations, the $TiC_{0.4}N_{0.6}$ measurement is not included in further evaluations.

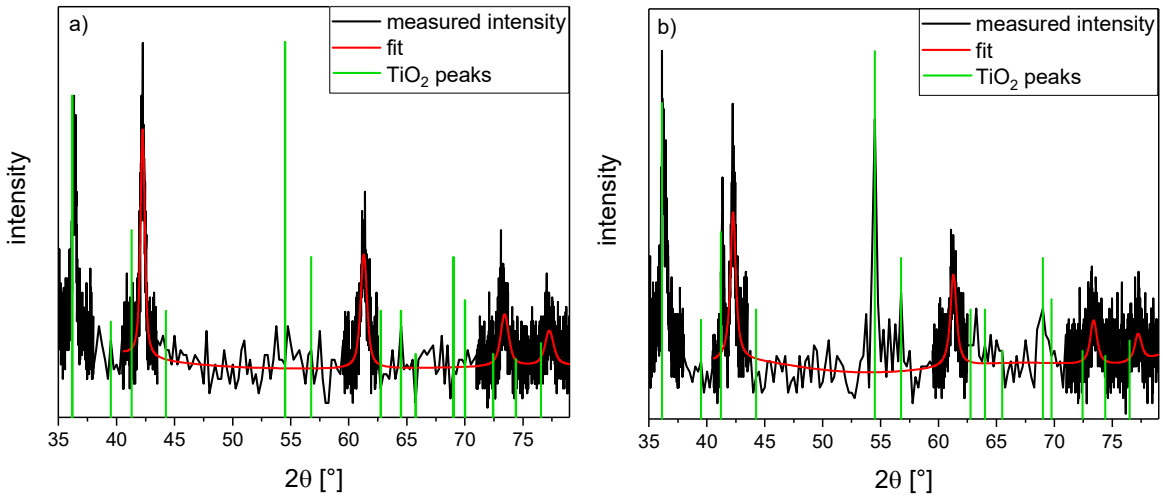

Figure 21: a) Diffractogram and fitted curve of $TiC_{0.4}N_{0.6}$ before the HT measurement but after recrystallization and b) after the complete measurement cycle. The possibly occurring TiO_2 (rutile) peaks are marked by the green vertical lines.

For the calculation of the TEC, the lattice parameters of the different Ti(C,N) were fitted by polynomial functions as shown for an example in Fig. 22. There, the averaged lattice parameters of the heating and cooling cycles of TiN and the fitted polynomial function are drawn in the temperature range of 25-1000 °C. Such polynomials were fitted to the averaged lattice parameters of every measured Ti(C,N) composition. The best fit could be achieved using parabolic functions of the type $a = A + B \cdot T + C \cdot T^2$, as it was reported in ref [42].

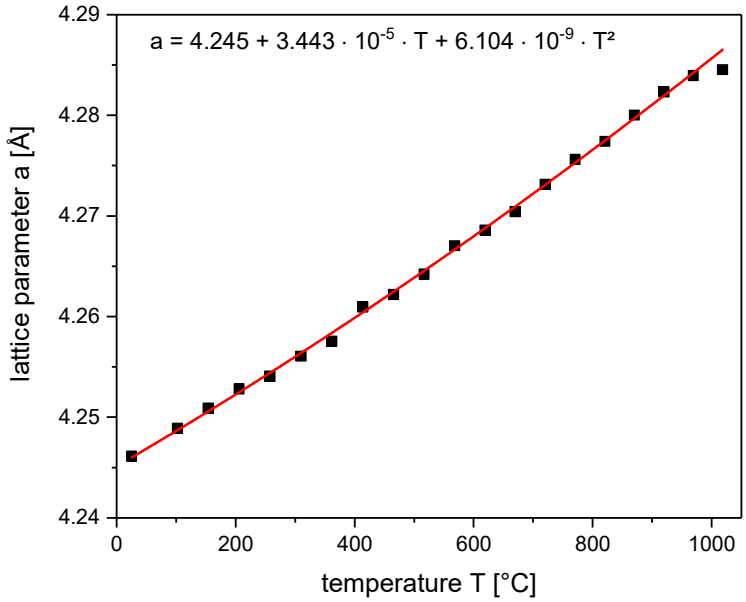

Figure 22: Averaged lattice parameters for TiN (symbols) calculated from the heating and cooling cycle and fitted polynomial function of the second order (line). The equation of the fitted function is written in the top of the graph.

After fitting all Ti(C,N) diffractograms, the compositions of the different samples were determined, by the assumption of a Vegard's like behavior [36]. According to that, there should be a linear change in lattice parameter with composition from TiN to TiC. This is drawn in Fig. 23 a) for the values calculated by the fitted parabolic functions at 25 °C for every sample. As comparison, literature values for TiN [33] and TiC [34] are also drawn in the graph. The differences to the literature values for TiN and TiC are indications for the presence of impurities, like C, N, O or other unwanted atoms in the measured samples, which affect the lattice parameter of sputtered materials. Figure 23 b) shows the difference of the fitted [C]/[C+N] ratio to the values determined by the assumption of a linear behavior. As can be seen, there is no trend in the deviations recognizable. Thus, the differences are

most probably due to the lattice parameter determination and errors in the sputter deposition process, like contamination of the targets or the chamber.

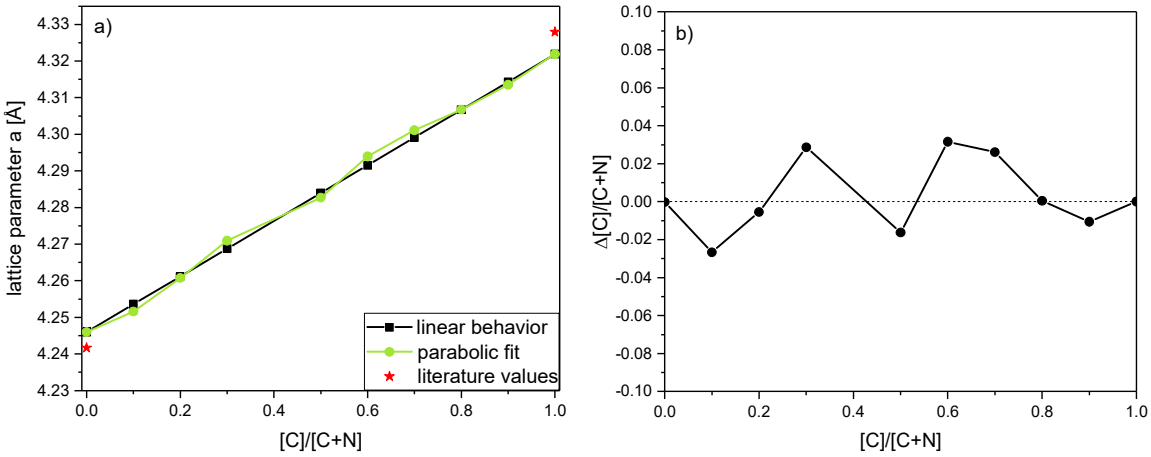

Figure 23: a) Lattice parameters of the different Ti(C,N) as a function of the [C]/[C+N] ratio calculated by the parabolic fitting functions at 25 °C compared to the values showing a hypothetical Vegard's like linear behavior between TiN and TiC, as well as the literature values for TiN [33] and TiC [34]. b) The difference of the fitted values to the ones showing linear behavior between the fitted TiN and TiC.

The determined compositions, as well as the lattice parameters at 25 °C of the different samples are listed in Table 3. The literature values for TiN and TiC are 4.2417 Å [33] and 4.3280 Å [34] and hence, they show differences of 0.0043 Å and 0.0061 Å, respectively. As these differences to literature values are approximately ten times the error determined by the Pt measurements, it cannot be a result of statistical deviations or temperature fluctuations resulting from the measurement. More likely, these rather high differences occur due to impurities, vacancies and other defects in the powder [37, 38, 40, 84]. As such defects are common in sputtered coatings, the determined compositions seem reliable.

Table 3: Determined compositions of the investigated Ti(C,N) powders in comparison to the supposed ones and lattice parameters at 25 °C calculated by the fitting functions.

Expected composition	Calculated composition	a [Å]
TiC	TiC	4.3219
$TiC_{0.9}N_{0.1}$	$TiC_{0.89}N_{0.11}$	4.3135
$TiC_{0.8}N_{0.2}$	$TiC_{0.80}N_{0.20}$	4.3067
$TiC_{0.7}N_{0.3}$	$TiC_{0.73}N_{0.27}$	4.3011
$TiC_{0.6}N_{0.4}$	$TiC_{0.63}N_{0.37}$	4.2939
$TiC_{0.5}N_{0.5}$	$TiC_{0.48}N_{0.52}$	4.2827
$TiC_{0.3}N_{0.7}$	$TiC_{0.33}N_{0.67}$	4.2710
$TiC_{0.2}N_{0.8}$	$TiC_{0.19}N_{0.81}$	4.2608
$TiC_{0.1}N_{0.9}$	$TiC_{0.07}N_{0.93}$	4.2516
TiN	TiN	4.2460

A summary of the measured Ti(C,N) values, including the fitted functions is given in Fig. 24 for all compositions and over the whole investigated temperature range. As expected, the lattice parameter increases with increasing carbon content from TiN to TiC and with increasing temperature.

In general, the errors and the differences between the up and down measurements are increasing with higher C content, especially for $TiC_{0.5}N_{0.5}$ - $TiC_{0.7}N_{0.3}$ as indicated by the increasing fluctuation of the recorded values (see Fig. 24). A reason for the more deviating values at higher C contents and especially at elevated temperatures can be, that during magnetron sputter deposition, the C of TiC may partly condense in form of graphite [84, 85]. This graphite most likely reacts to CO_2 or CO during the HT measurement with the incorporated O in the powder and the available O_2 in the capillary atmosphere at temperatures exceeding 400 °C [86]. Another reason for the deviations may be, that especially for elevated C contents the powder showed higher tendency to agglomerate and hence, got stuck in the upper part of the capillaries, as the diameter decreases to the capillary tip. Hence, for some of the compositions, the capillaries could not be filled in the complete range of the measuring X-ray beam, resulting in possible errors.

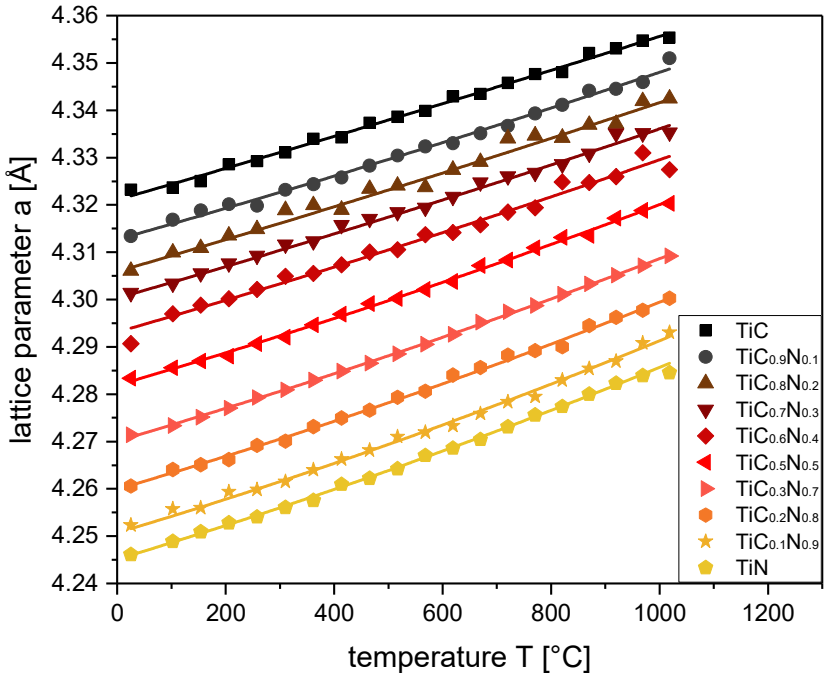

Figure 24: Recorded lattice parameters of the different Ti(C,N) powders for the temperature range of 25 to 1000 °C (symbols) and the fitted parabolic functions (lines).

With the calculated compositions in Table 3, the graphs in Fig. 25 a-c) were drawn. These graphs show the three coefficients *A*, *B* and *C* of the parabolic fitting functions, determined for the different Ti(C,N) lattice parameters over the complete temperature range, like in Fig. 22. As can be seen, all coefficients show an approximately linear trend over the whole compositional range. Hence, all three coefficients can be fitted by a linear function. The first coefficient is the lattice parameter at 0 °C. As the correct compositions of the different samples were calculated assuming a Vegard's like behavior at 25 °C, it is clear that these coefficients exhibit a nearly perfect linear behavior. The only minor deviations arise from the different thermal expansions between 0 and 25 °C. Coefficient *B* represents the slope of the fits at 0 °C. The falling trend of *B* from TiN to TiC results from a decreasing TEC at low temperatures with increasing *C* content. The third coefficient, indicating the temperature dependence of the TEC, also shows a negative slope from TiN to TiC. This is an indication for an increasing difference in thermal expansion with higher temperature from TiN to TiC.

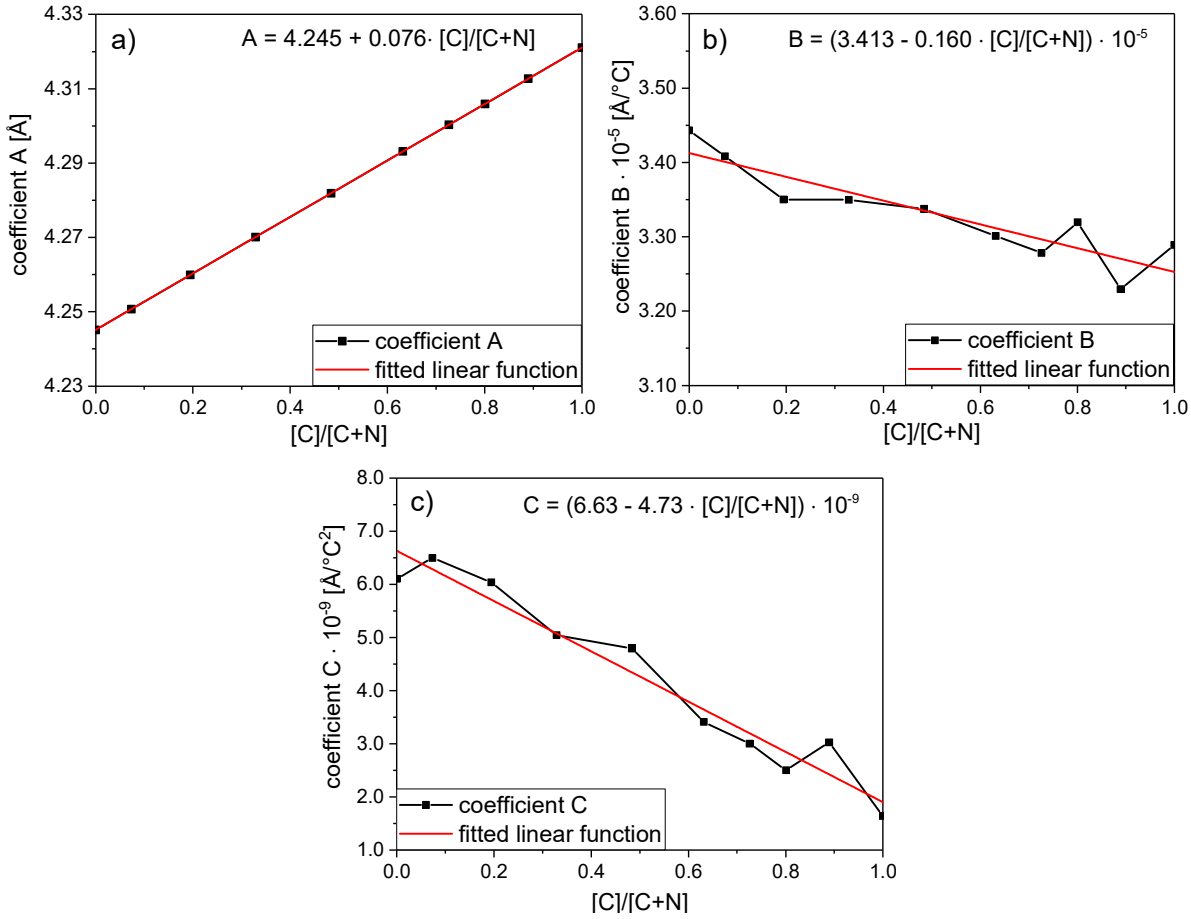

Figure 25: Coefficients *A*, *B* and *C* of the different Ti(C,N) lattice parameter fits, drawn over the [C]/[C+N] ratio, including the linear fitting functions in the top of the graphs.

By combining these three linear functions to a parabolic fitting function similar to those for the different Ti(C,N) compositions, the polynomial equation

$$a_{\left(\frac{[C]}{[C]+[N]},T\right)} = 4.245 + 0.076 \cdot \frac{[C]}{[C]+[N]} + \left(3.413 - 0.160 \cdot \frac{[C]}{[C]+[N]}\right) \cdot 10^{-5} \cdot T + \left(6.63 - 4.73 \cdot \frac{[C]}{[C]+[N]}\right) \cdot 10^{-9} \cdot T^2 \qquad (11)$$

for the temperature and composition dependent lattice parameter can be deduced, where *T* is the temperature in °C. This function allows to calculate the lattice parameter of Ti(C,N) at any given composition ranging from pure TiN to pure TiC, in the temperature range of 25 to 1000 °C.

With the developed eq. 11, the lattice parameters can be calculated and displayed for comparison to the results of other studies, as exemplified in Fig. 26. There the values are drawn for four different compositions in comparison to the lattice parameters calculated by eq. 1 from Aigner *et al.* [42]. As can be seen, the values obtained in this thesis differ considerably (up to 0.01 Å) from those reported by Aigner *et al.* While at low C contents, i.e.

close to TiN, the lattice parameter of Aigner *et al.* is smaller than the values reported here, at high C contents (above approximately 60 at.% C) the opposite trend was observed. This might be due to the following reasons:

1. The powders in ref. [42] were produced by ball milling and hot pressing a combination of Ti, TiN and TiC powder, at a temperature of 2800 K and a pressure of 55 MPa, to achieve nearly dense samples. These samples were crushed and again ball milled afterwards. As the Ti(C,N) results from diffusion processes during the pressing step, some inhomogeneity such as clusters of TiN and TiC might still be present in the investigated powder. Such inhomogeneity should not occur in the samples prepared by magnetron sputtering, as within this technique the different atoms or molecules condense individually on the rotating substrate.
2. The TiN and TiC sputter targets used in this work had a purity of 99.5 %, comparable to the TiN and TiC in [42]. However, the difference is, that the remaining 0.5 % of the sputter targets are unknown and thus, they possibly have some influence on the lattice parameter compared to the powder used in ref. [42]. There it is known that the remaining 0.5 % are C and N, respectively.
3. Ar and O incorporations as well as different defects in the coating can change the lattice parameter of the sputter deposited powder significantly, like mentioned above, compared to hot pressed and ball milled samples [40, 84]. Whereas during ball milling, other contaminations and impurities, like abrasion products of the milling balls, can pollute the material [87].
4. The powders in ref. [42] were measured by XRD in reflection geometry, spread with methanol on a tantalum strip as sample holder. The ambient gas was He and the diffractograms were fitted by Pearson VII functions. Due to these dissimilarities of the experimental setup, also differences of the lattice parameter could have occurred.

Nonetheless, the results of the lattice parameter measurements are to a large extent in good agreement with the existing data.

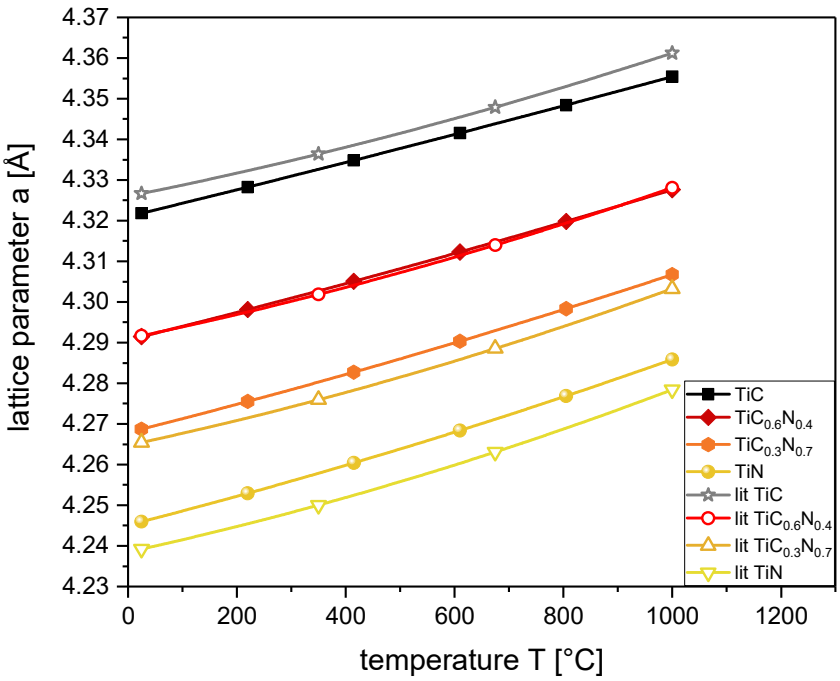

Figure 26: Lattice parameters calculated by eq. 11 for [C]/[C+N] = 0, 0.3, 0.6 and 1, compared to the values, calculated by the equation from literature eq. 1 for the same compositions [42].

With eq. 11, the difference in lattice parameters between the fit and the $TiC_{0.4}N_{0.6}$ measurement can be displayed in Fig. 27. This demonstrates the influence of oxidation on the lattice parameter of the sample. The recorded curve exhibits a much higher temperature dependence of the gradient compared to the calculated one. Hence, an increasing difference of up to nearly 0.02 Å at elevated temperatures arises, which is far more than the errors for the other compositions. This difference in lattice parameter is most probably a result of the higher lattice constant of TiO_2 (4.594 Å [79]), compared to the ones of TiN and TiC, as incorporated TiO_2 in the Ti(C,N) particles may have an influence on the thermal expansion.

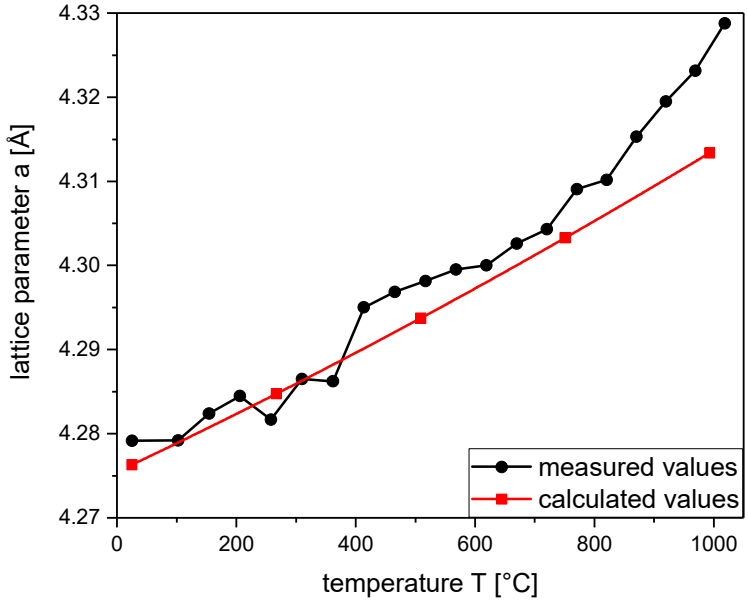

Figure 27: Comparison of recorded lattice parameters of the $TiC_{0.4}N_{0.6}$ sample by HT X-ray diffraction to calculated ones by eq. 11.

Linear thermal expansion coefficient of Ti(C,N)

As the TEC of Ti(C,N) varies as a function of the temperature, which is indicated by the change of the gradient of the lattice parameter curves, the linear TEC α in $°C^{-1}$ can be determined as a function of the temperature and the [C]/[C+N] ratio, using

$$\alpha_{\left(\frac{[C]}{[C]+[N]},T\right)} = \frac{da_{\left(\frac{[C]}{[C]+[N]},T\right)}}{dT} \cdot \frac{1}{a_{\left(\frac{[C]}{[C]+[N]},T\right)}}. \quad (12)$$

Inserting eq. 11 in eq. 12, results in

$$\alpha_{\left(\frac{[C]}{[C]+[N]},T\right)} = \frac{\left(3.413-0.160\cdot\frac{[C]}{[C]+[N]}\right)\cdot 10^{-5}+\left(1.326-0.946\cdot\frac{[C]}{[C]+[N]}\right)\cdot 10^{-8}\cdot T}{4.245+0.076\cdot\frac{[C]}{[C]+[N]}+\left(3.413-0.160\cdot\frac{[C]}{[C]+[N]}\right)\cdot 10^{-5}\cdot T+\left(6.63-4.73\cdot\frac{[C]}{[C]+[N]}\right)\cdot 10^{-9}\cdot T^2}. \quad (13)$$

This equation allows to calculate the linear TEC of Ti(C,N) in the temperature range of 25-1000 °C. The function is plotted in Fig. 28 for [C]/[C+N] ratios from 0 to 1 in steps of 0.1 over the complete investigated temperature range. There, the TEC increases from TiC to TiN. This trend correlates with the melting points of TiC and TiN, which are 3140 °C and 2930 °C, respectively [79], as the TEC and the melting point show inversely proportional behavior for cubic materials [88]. The TEC also increases nearly linear with temperature for the whole compositional range, whereby TiN exhibits a higher gradient in α than TiC.

For comparison the linear TECs for TiN and TiC, calculated by eq. 3 [42][1], are also drawn in the graph. The results from [42] obviously exhibit a higher variation in α over the temperature, than the curves determined in this work, leading to a difference of up to $1.7 \cdot 10^{-6}$ °C^{-1} at 1000 °C for TiC, for example. These differences most probably can be explained by the same reasons as discussed for the lattice parameters in Fig. 26.

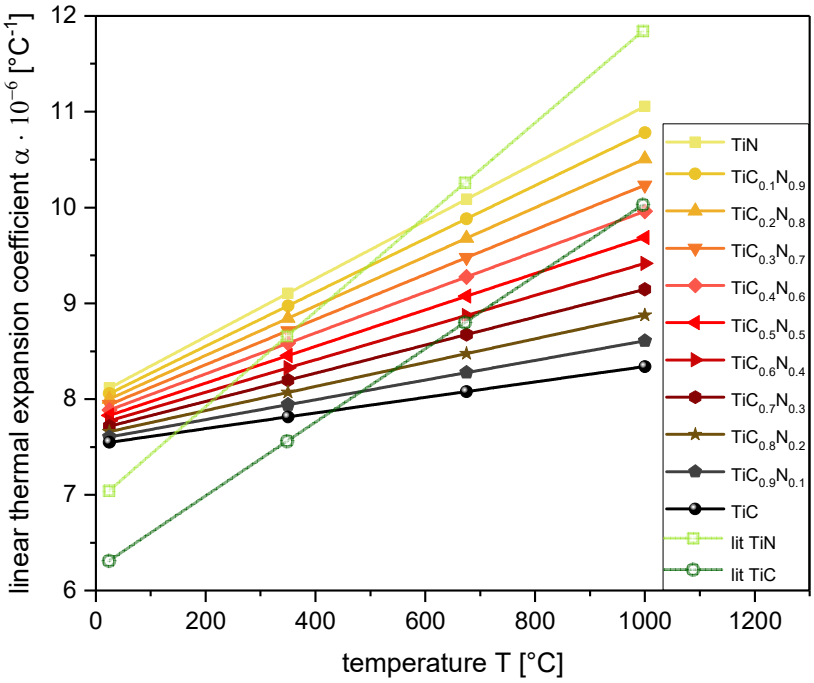

Figure 28: Linear TEC, calculated using eq. 13 for [C]/[C+N] ratios varying from 0 to 1 in steps of 0.1, in comparison to TiC and TiN, calculated by eq. 3 [42][1], in the temperature range of 25 to 1000 °C.

Fig. 29 represents a 3D plot of the linear TEC calculated using eq. 13. The curvature of the plane indicates that the TEC increases stronger at lower temperatures than at higher temperatures. This trend is in agreement with the calculated results reported by Kim *et al.* [43]. The difference of their results, determined by ab initio calculations for defect free materials to the linear TEC in Fig. 29, however, is that they found a much greater temperature dependence of the TEC (especially below 300 °C) than observed in this work. At higher temperatures, both, the gradient and the curvature decrease and do have similar values to the ones shown in Figs. 28 and 29. Nevertheless, the TEC itself exhibit quite lower values over the complete temperature range in [43], lying between $\alpha = 5 \cdot 10^{-6}$ °C^{-1} and

[1] Equation 3 taken from [42] exhibits a typo. The plus in the right parentheses should be a minus, like in eq. 13. This was corrected for in the calculation of α for Fig. 28.

$\alpha = 8 \cdot 10^{-6}$ °C^{-1}. These differences can most likely be attributed to the assumption of defect free materials for the calculation, which is not the case in sputtered materials typically showing highly defective structures [43].

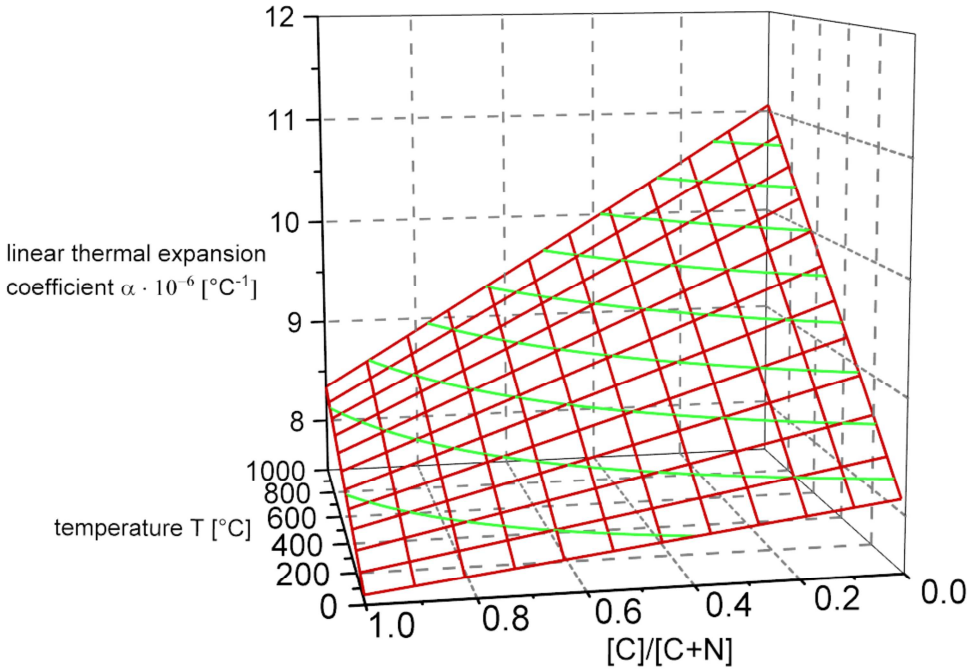

Figure 29: Linear TEC α, as a function of the [C]/[C+N] ratio and the temperature. The green lines represent ranges of constant α on the surface.

With the temperature dependent lattice parameter, the linear thermal expansion of the Ti(C,N) starting from 25 °C, can be calculated using

$$\frac{\Delta a}{a_0\left(\frac{[C]}{[C+N]},T\right)} = \frac{a_{\left(\frac{[C]}{[C+N]},T\right)} - a_{\left(\frac{[C]}{[C+N]},25\right)}}{a_{\left(\frac{[C]}{[C+N]},25\right)}}. \quad (14)$$

This function is plotted in Fig. 30 for six different [C]/[C+N] ratios between zero and one, in equal steps of 0.2. Like estimated from the linear TEC in Fig. 28, the thermal expansion increases from TiC to TiN. At 1000 °C, the smallest thermal expansion is 0.78 % for TiC and the highest is 0.94 % for TiN.

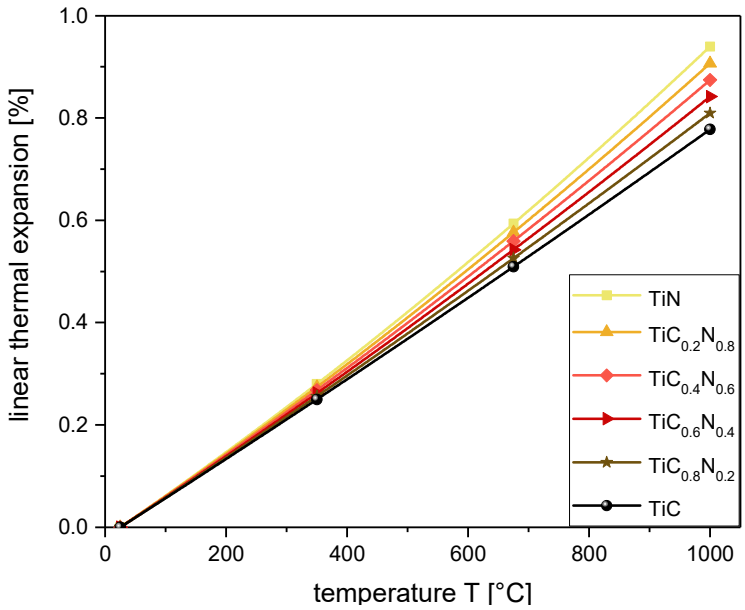

Figure 30: Linear thermal expansion of Ti(C,N) with [C]/[C+N] ratios varying from 0 to 1 in steps of 0.2, in the temperature range of 25 to 1000 °C.

As comparison to already existing results for hot pressed Ti(C,N), the thermal expansions for TiN and TiC determined in this work and the ones from refs. [41, 42] are displayed in Fig. 31. The sputtered TiN exhibits the highest thermal expansion over the complete temperature range, whereas for TiC the values from literature are nearly the same. In general, the data reported in ref. [42] shows a lower thermal expansion at low temperatures, which is increasing to nearly the same values as for the sputtered samples at high temperatures. The data reported in ref. [41] shows a lower expansion for TiN, but nearly the same for TiC compared to the values for the sputtered samples. Hence, the difference between the carbide and the nitride is much smaller than for the other curves, especially at elevated temperatures. As the thermal expansion was not measured at temperatures below 750 °C in ref. [41], there is no information for low temperatures. The difference, especially to the values for the sputtered TiN from ref. [41], may be stemming from the sample production and evaluation, which was performed by pressing and sintering TiN and TiC powder to bulk materials. These were measured in a HT X-ray diffractometer furnace. Also the purity of the samples can have an influence on the thermal expansion [41].

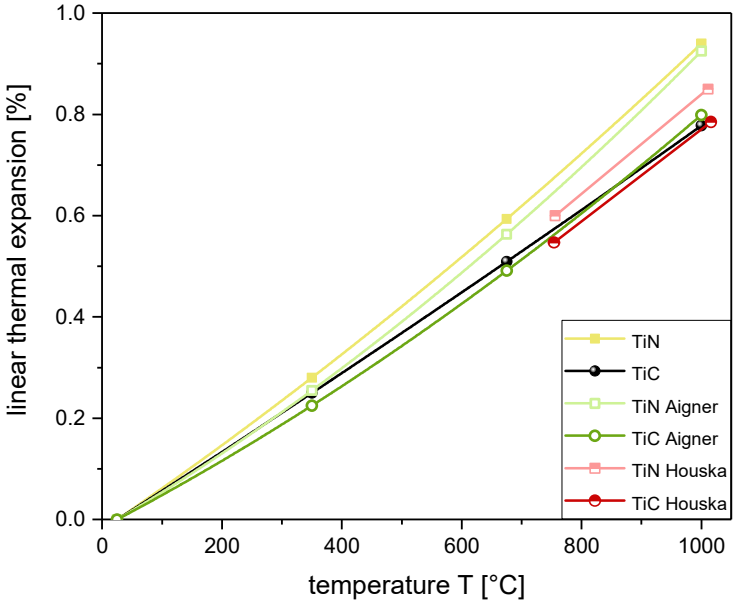

Figure 31: Linear thermal expansion of TiN and TiC determined in this work in comparison to the values for TiN and TiC reported by Aigner *et al.* [42] and Houska [41] in the temperature range of 25 to 1000 °C.

Average thermal expansion coefficient of Ti(C,N)

From the lattice parameters of the Ti(C,N) powders in the mentioned temperature range, the average TEC can be calculated. This is done by fitting the lattice parameter curves with linear functions, and calculating the TEC by

$$\alpha_{\left(\frac{[C]}{[C+N]}\right)} = \frac{da_{lin\left(\frac{[C]}{[C+N]}\right)}}{dT} \cdot \frac{1}{a_{lin\left(\frac{[C]}{[C+N]},T=25\right)}}, \tag{15}$$

which is plotted in Fig. 32. Here, $da_{lin\left(\frac{[C]}{[C+N]}\right)}/dT$ is the gradient of the linear fitting curves and $a_{lin\left(\frac{[C]}{[C+N]},T=25\right)}$ is the lattice parameter at 25 °C of the different Ti(C,N) compositions. It is evident, that the average TEC in °C^{-1} between TiN and TiC exhibits a nearly linear behavior over the whole composition and thus, it can be fitted by the linear equation

$$\alpha_{av\left(\frac{[C]}{[C+N]}\right)} = \left(9.61 - 1.63 \cdot \frac{[C]}{[C+N]}\right) \cdot 10^{-6}. \tag{16}$$

The deviation at [C]/[C+N] ~ 0.7 most likely is a result of fitting errors, stemming from the rather high fluctuation of the lattice parameters at this composition. For comparison, the average TEC determined by eq. 2 from Aigner *et al.* [42] is also drawn in the graph. The expansion coefficients calculated by the literature equation show higher values over the total compositional range, with an increasing difference from $0.32 \cdot 10^{-6}$ °C^{-1} for TiN to

$0.50 \cdot 10^{-6}$ °C^{-1} for TiC. However, the curves exhibit nearly the same dependence on the composition of the Ti(C,N). The reason for the difference is that eq. 2 was determined for the temperature range of 25-1200 °C. As the linear TEC in [42] does not exhibit a linear temperature dependence, the average TEC varies depending on the investigated temperature range. Thus, the function changes when determined for a different temperature range, like 25-1000 °C as in this work.

The described results of polycrystalline powder do not agree with the function of the average TEC, reported in [44] for Ti(C,N) whiskers, which were measured with a X-ray diffractometer in Bragg-Brentano geometry. Their results also show a reduction in α_{av} with increasing C content, starting from $9.4 \cdot 10^{-6}$ K^{-1} for TiN, down to around $7.5 \cdot 10^{-6}$ K^{-1} for $TiC_{0.6}N_{0.4}$, but then the trend is changing and the value is rising up to $8.5 \cdot 10^{-6}$ K^{-1} for TiC. This difference is most likely a consequence of the fact, that a whisker is a single crystal with hardly any grain boundaries and defects, like dislocations and impurities. In contrary, polycrystalline powder normally shows a high amount of defects and grain boundaries.

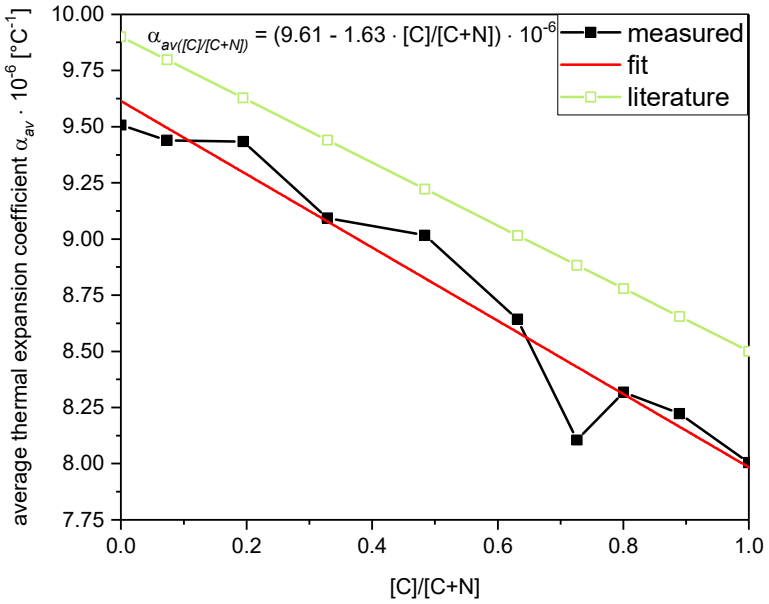

Figure 32: Average thermal expansion coefficients α_{av} determined for the temperature region of 25 to 1000 °C for the measured samples, fitted by a linear function $\alpha_{av([C]/[C+N])}$, in comparison to the values calculated by eq. 2 [42].

To give a short overview of the determined results, the average TECs are summarized in table 4 over the complete [C]/[C+N] range in steps 0.1, determined by eq. 16.

Table 4: Overview of average thermal expansion coefficients of Ti(C,N)

composition	α_{av} [°C^{-1}]
TiN	9.61
$TiC_{0.1}N_{0.9}$	9.45
$TiC_{0.2}N_{0.8}$	9.28
$TiC_{0.3}N_{0.7}$	9.12
$TiC_{0.4}N_{0.6}$	8.96
$TiC_{0.5}N_{0.5}$	8.80
$TiC_{0.6}N_{0.4}$	8.63
$TiC_{0.7}N_{0.3}$	8.47
$TiC_{0.8}N_{0.2}$	8.31
$TiC_{0.9}N_{0.1}$	8.14
TiC	7.98

Comparison with Ti(C,N) synthesized by CVD

As comparison to the evaluated Ti(C,N) synthesized by magnetron sputtering, two different powders produced by CVD were also measured by HT XRD. One of the samples was pure TiN and the other was a Ti(C,N) coating with unknown composition. To determine the actual compositions, the lattice parameters were compared to the literature values of TiN [33] and TiC [34] assuming a linear Vegard's like behavior, as can be seen in Fig. 33. There, the lattice parameters of the CVD samples, the literature values and the values calculated by eq. 11 are drawn as a function of the [C]/[C+N] ratio. It can be seen, that the TiN synthesized by CVD exhibits nearly the same lattice parameter as in [33], leading to a small difference of approximately 0.016 in [C]/[C+N]. The composition determined for the CVD Ti(C,N) is $TiC_{0.54}N_{0.46}$.

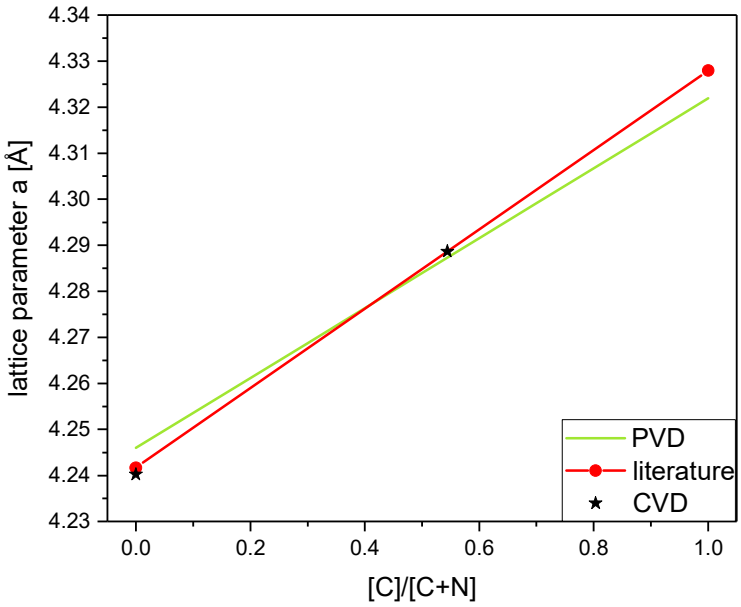

Figure 33: Lattice parameters of TiN and Ti(C,N), synthesized by CVD, as a function of the [C]/[C+N] ratio compared to the values calculated from literature values for TiN and TiC assuming a Vegard's like behavior and the lattice parameters calculated by eq. 11 at 25 °C of Ti(C,N) synthesized by sputtering.

Comparing the parabolic fits of the lattice parameters as functions of the temperature for the magnetron sputtered and CVD samples, it is evident, that they exhibit a similar dependence on the temperature, as displayed in Fig. 34. The sputtered curves were calculated by eq. 11 for [C]/[C+N] ratios of 0 and 0.54. Looking at the two $TiC_{0.54}N_{0.46}$ curves, it can be seen that they only exhibit a very small difference, which most probably results from different defect densities of the samples. As the differences between the TiN curves are approximately the same as compared to ref. [42], shown in Fig. 26, it can be assumed, that they are also stemming from defects and impurities and not from measurement errors.

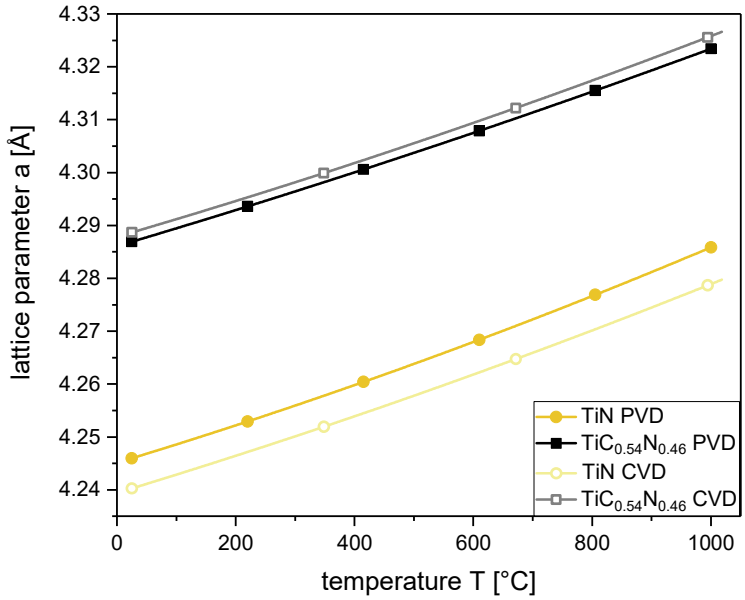

Figure 34: Comparison of the parabolic lattice parameter fits of TiN and $TiC_{0.54}N_{0.46}$, synthesized by CVD, to the calculated PVD lattice parameters by eq. 11 in the temperature range of 25 to 1000 °C.

By fitting the lattice parameters with linear functions, the average TECs can be determined and compared to the sputtered ones, calculated by eq. 16. These are drawn in Fig. 35 as functions of the [C]/[C+N] ratio. As the values of the chemical vapor deposited materials lie in the fluctuation range of the values for the sputtered materials, compared to Fig. 32, the differences most probably are statistical errors. Thus the determined average TECs of the magnetron sputtered Ti(C,N) coatings seem to correlate well with CVD synthesized materials.

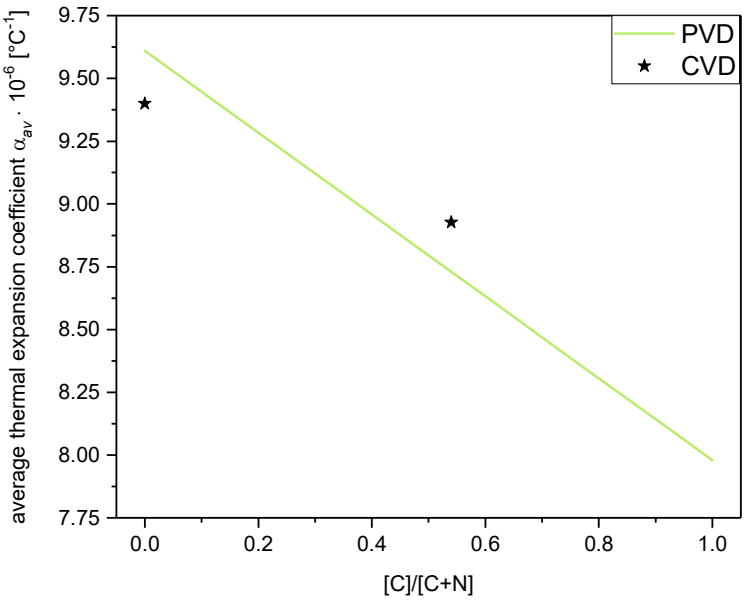

Figure 35: Average TEC of CVD TiN and $TiC_{0.54}N_{0.46}$ compared to the values calculated by eq. 13 for PVD powder.

5 Summary and Conclusions

The aim of this study was to investigate the thermal expansion of nonreactively magnetron sputtered Ti(C,N) powders with different compositions, varying from pure TiN to pure TiC in equal steps of 0.1. The temperature range, in which the Ti(C,N) coatings were investigated, was 25 to 1000 °C. The used measurement method was high temperature X-ray diffraction in transmission mode and the diffractograms were evaluated by the refinement of the lattice parameters with space group based models. The high temperature chamber was first calibrated by the measurement of the temperature dependent lattice parameter of Pt, temperature recording with a thermocouple and the determination of the melting points of different metals. From the average lattice parameters of five different Pt measurements, the temperature difference to the set values was evaluated by comparison with a temperature dependent literature function of the Pt lattice parameter. This temperature difference, which was rising with increasing temperature up to a level of about 800 °C, was used to correct the set temperature for further evaluations. The developed correction curve could be confirmed by the thermocouple measurement, which showed the same trend in ΔT as calculated by the Pt calibration. The determination of the melting points did not provide valid results.

The investigation of the Ti(C,N) powders resulted in lattice parameters dependent on the temperature, rising with composition from TiN to TiC. The exact compositions of the powders were determined assuming a Vegard's like behavior between TiN and TiC. The obtained values for the lattice parameter were fitted by parabolic functions, which were combined to an equation for the lattice parameter, dependent on the temperature and the [C]/[C+N] ratio. Out of this the function for the linear TEC could be determined by differentiation of the lattice parameter equation. In general, the TEC exhibits a decreasing value with increasing C content. The temperature dependence is depicted by a rising TEC with elevating temperature, going from $7.55 \cdot 10^{-6}\,°C^{-1}$ to $8.34 \cdot 10^{-6}\,°C^{-1}$ for TiC and from $8.12 \cdot 10^{-6}\,°C^{-1}$ to $11.06 \cdot 10^{-6}\,°C^{-1}$ for TiN in the investigated temperature range. By linear fitting of the measured values, the average TEC could be determined as a function of [C]/[C+N]. This average TEC exhibits a linear behavior, decreasing from $9.61 \cdot 10^{-6}\,°C^{-1}$ for TiN to $7.98 \cdot 10^{-6}\,°C^{-1}$ for TiC, which is in good agreement with literature data. Reviewing the developed functions, a nearly linear behavior for the lattice parameters, as well as for the

TEC was observed, rising from TiC to TiN. In comparison to sintered or hot pressed Ti(C,N), the sputtered Ti(C,N) coatings exhibit a TEC with a smaller change over the temperature.

Finally it can be said, that within this work reliable temperature dependent equations for the lattice parameters, as well as the thermal expansion coefficients of magnetron sputtered Ti(C,N) could be determined using high temperature X-ray diffraction. Up to now, comparable data on Ti(C,N) could only be found for hot pressed samples and single crystals but not for deposited materials. Thus, the gained results close an important gap in the knowledge for improving the properties of multilayered coatings containing Ti(C,N), especially where it is used as base layer to compensate for the thermal expansion of substrate and coating.

6 Literatur

1 *S. Dolinšek, B. Šuštaršič, J. Kopač*, Wear mechanisms of cutting tools in high-speed cutting processes, Wear 250 (2001) 349–356

2 *C. Ducros, V. Benevent, F. Sanchette*, Deposition, characterization and machining performance of multilayer PVD coatings on cemented carbide cutting tools, Surf. Coat. Technol. 163–164 (2003) 681–688

3 *P. C. Jindal, A. T. Santhanam, U. Schleinkofer, A. F. Shuster*, Performance of PVD TiN, TiCN, and TiAlN coated cemented carbide tools in turning, Int. J. Refract. Met. Hard Mater. 17 (1999) 163–170

4 *H. Holleck, V. Schier*, Multilayer PVD coatings for wear protection, Surf. Coat. Technol. 76–77 (1995) 328–336

5 *S. J. Bull, D. G. Bhat, M. H. Staia*, Properties and performance of commercial TiCN coatings. Part 1: coating architecture and hardness modelling, Surf. Coat. Technol. 163–164 (2003) 499–506

6 *S. J. Bull, D. G. Bhat, M. H. Staia*, Properties and performance of commercial TiCN coatings. Part 2: tribological performance, Surf. Coat. Technol. 163–164 (2003) 507–514

7 *J. Deng, M. Braun, I. Gudowska*, Properties of TiCN coatings prepared by magnetron sputtering, J. Vac. Sci. Technol., A 12 (1994) 733–736

8 *L. F. Senna, C. A. Achete, T. Hirsch, F. L. Freire*, Structural, chemical, mechanical and corrosion resistance characterization of TiCN coatings prepared by magnetron sputtering, Surf. Coat. Technol. 94–95 (1997) 390–397

9 *R. Haubner, B. Lux*, Diamond deposition on steel substrates using intermediate layers, Int. J. Refract. Met. Hard Mater. 24 (2006) 380–386

10 *C. Czettl, C. Mitterer, U. Mühle, D. Rafaja, S. Puchner, H. Hutter, M. Penoy, C. Michotte, M. Kathrein*, CO addition in low-pressure chemical vapour deposition of medium-temperature TiC_xN_{1-x} based hard coatings, Surf. Coat. Technol. 206 (2011) 1691–1697

11 *K. Okushima, K. Hitomi K.*, A study of economical machining: An analysis of the maximum-profit cutting speed, Int. J. Prod. Res. 3 (1964) 73–78

12 *N. A. Abukhshim, P. T. Mativenga, M. A. Sheikh*, Heat generation and temperature prediction in metal cutting: A review and implications for high speed machining, Int. J. Mach. Tool. Manu. 46 (2006) 782–800

13 *H. Holleck*, Material selection for hard coatings, J. Vac. Sci. Technol., A 4 (1986) 2661–2669

14 *D. Bandyopadhyay, R. C. Sharma, N. Chakraborti*, The Ti-N-C system (titanium - nitrogen - carbon), J. Phase Equilib. 21 (2000) 192–194

15 *L. F. S. Dumitrescu, M. Hillert, B. Sundman*, A Reassessment of Ti-C-N based on a Critical Review of Available Assessments of Ti-N and Ti-C, Metallkunde (1999) 534–541

16 *K. Wasa, I. Kanno, H. Kotera*, Handbook of Sputter Deposition Technology, Fundamentals and applications for functional thin films, nano-materials and MEMS, Elsevier/Andrew, Amsterdam 2012, pp. 96–101

17 *R. A. Haefer*, Oberflächen- und Dünnschicht-Technologie, Teil 1: Beschichtungen von Oberflächen, Springer-Verlag, Berlin 1987, pp. 4–7, 95–120

18 *R. F. Bunshah*, Handbook of Deposition Technologies for Films and Coatings, Science, technology, and applications, Noyes Publications, Park Ridge, New Jersey 1994, pp. 276–335

19 *B. Chapman*, Glow Discharge Processes, Sputtering and Plasma Etching, Wiley, New York 1980, pp. 188–190, 260–270

20 *P. J. Kelly, R. D. Arnell*, Magnetron sputtering: a review of recent developments and applications, Vacuum 56 (2000) 159–172

21 *W. D. Sproul*, Multi-cathode unbalanced magnetron sputtering systems, Surf. Coat. Technol. 49 (1991) 284–289

22 *W. D. Sproul*, Ion-assisted deposition in unbalanced-magnetron sputtering systems, Mater. Sci. Eng., A 163 (1993) 187–192

23 *P. Mayrhofer*, Materials Science Aspects of Nanocrystalline PVD Hard Coatings, PhD-thesis, University of Leoben, Leoben, 2001

24 *Gupta S., Glocker D., Romach M.*, Nanoindentation and X-ray Diffraction Study of Sputtered TiCN Coatings, Microsc. Microanal. 10 (2004) 602–603

25 *S. Vepřek, M. Haussmann, S. Reiprich, L. Shizhi, J. Dian*, Novel thermodynamically stable and oxidation resistant superhard coating materials, Surf. Coat. Technol. 86–87 (1996) 394–401

26 *J. C. Caicedo, C. Amaya, L. Yate, M. E. Gómez, G. Zambrano, J. Alvarado-Rivera, J. Muñoz-Saldaña, P. Prieto*, TiCN/TiNbCN multilayer coatings with enhanced mechanical properties, Appl. Surf. Sci. 256 (2010) 5898–5904

27 *C. Subramanian, K. N. Strafford*, Review of multicomponent and multilayer coatings for tribological applications, Wear 165 (1993) 85–95

28 *R. Chen, J. P. Tu, D. G. Liu, Y. J. Mai, C. D. Gu*, Microstructure, mechanical and tribological properties of TiCN nanocomposite films deposited by DC magnetron sputtering, Surf. Coat. Technol. 205 (2011) 5228–5234

29 *P. Villars, L. D. Calvert*, Pearson's Handbook of Crystallographic Data for Intermetallic Phases, American Society for Metals, Metals Park, Ohio 1985

30 *A. A. Adjaottor, E. I. Meletis, S. Logothetidis, I. Alexandrou, S. Kokkou*, Effect of substrate bias on sputter-deposited TiC_x, TiN_y and TiC_xN_y thin films, Surf. Coat. Technol. 76–77 (1995) 142–148

31 *G. Levi, W. D. Kaplan, M. Bamberger*, Structure refinement of titanium carbonitride (TiCN), Mater. Lett. 35 (1998) 344–350

32 *G. Effenberg, S. Ilyenko*, Ternary Alloy Systems - Phase Diagramms, Carbon-Nitrogen-Titanium, Landolt-Börnstein, New Series IV/11A4, Springer-Verlag, Berlin 2006, pp. 121–131

33 *International Centre for Diffraction Data, Card 00-038-1420 for TiN*

34 *International Centre for Diffraction Data, Card 01-071-0298 for TiC*

35 *J. M. Schneider, A. Voevodin, C. Rebholz, A. Matthews, J. H. C. Hogg, D. B. Lewis, M. Ives*, X-ray diffraction investigations of magnetron sputtered TiCN coatings, Surf. Coat. Technol. 74–75 (1995) 312–319

36 *L. Vegard*, Die Konstitution der Mischkristalle und die Raumfüllung der Atome, Z. Phys. 5 (1921) 17–26

37 *D. S. Rickerby, A. M. Jones, B. A. Bellamy*, X-ray diffraction studies of physically vapour-deposited coatings, Surf. Coat. Technol. 37 (1989) 111–137

38 *V. Valvoda, R. Kužel, R. Černý, L. Dobiášová*, Detailed X-ray diffraction study of titanium nitride coatings: Some interpretation problems, Mater. Sci. Eng., A 104 (1988) 223–234

39 *A. J. Perry, M. Jagner, W. D. Sproul, P. J. Rudnik*, The residual stress in TiN films deposited onto cemented carbide by high-rate reactive sputtering, Surf. Coat. Technol. 39–40 (1989) 387–395

40 *J. E. Sundgren*, Structure and properties of TiN coatings, Thin Solid Films 128 (1985) 21–44

41 *C. R. Houska*, Thermal expansion and atomic vibration amplitudes for TiC, TiN, ZrC, ZrN, and pure tungsten, J. Phys. Chem. Solids 25 (1964) 359–366

42 *K. Aigner, W. Lengauer, D. Rafaja, P. Ettmayer*, Lattice parameters and thermal expansion of $Ti(C_xN_{1-x})$, $Zr(C_xN_{1-x})$, $Hf(C_xN_{1-x})$ and TiN_{1-x} from 298 to 1473 K as investigated by high-temperature X-ray diffraction, J. Alloys Compd. 215 (1994) 121–126

43 *J. Kim, S. Kang*, Elastic and thermo-physical properties of TiC, TiN, and their intermediate composition alloys using ab initio calculations, J. Alloys Compd. 528 (2012) 20–27

44 *K. Wokulska*, Thermal expansion of whiskers of Ti(C,N) solid solutions, J. Alloys Compd. 264 (1998) 223–227

45 *W. H. Zhang, J. H. Hsieh*, Tribological behavior of TiN and CrN coatings sliding against an epoxy molding compound, Surf. Coat. Technol. 130 (2000) 240–247

46 *T. Polcar, R. Novák, P. Široký*, The tribological characteristics of TiCN coating at elevated temperatures, Wear 260 (2006) 40–49

47 *J. H. Hsieh, A. L. K. Tan, X. T. Zeng*, Oxidation and wear behaviors of Ti-based thin films, Surf. Coat. Technol. 201 (2006) 4094–4098

48 *R. Allmann*, Röntgen-Pulverdiffraktometrie, Springer-Verlag, Berlin 2003, pp. 7–8

49 *B. D. Cullity, S. T. Stock*, Elements of X-ray Diffraction, Prentice Hall, Upper Saddle River, New jersey 2001

50 *K. H. Jost*, Röntgenbeugung an Kristallen, Heyden & Sohn, Rheine 1975

51 *R. E. Dinnebier, S. J. L. Billinge*, Powder Diffraction, Theory and Practice, RSCPublishing, Cambridge 2008

52 *L. Spieß, G. Teichert, R. Schwarzer, H. Behnken, C. Genzel*, Moderne Röntgenbeugung, Vieweg+Teubner, Wiesbaden 2009

53 *M. Dapiaggi, G. A. Petras, L. Petras*, A newly developed high-temperature chamber for in-situ X-Ray diffraction: Setup and calibration procedures, Rigaku Journal 19 (2002) 35–41

54 *P. Ramminger, R. Tessadri, R. Krismer, P. Wilhartitz*, Application of high temperature x-ray diffraction as a tool for material characterization and product optimization, in Proceedings of the 15th International Plansee Seminar, Reutte, Austria, Plansee Holding AG, 2001, pp. 216–228

55 *A. Kern*, Hochtemperatur-Rietveldanalyse: Möglichkeiten und Grenzen, PhD-thesis, Ruprecht-Karls-Universität, Heidelberg, 1998

56 *J. Keckes, M. Bartosik, R. Daniel, C. Mitterer, G. E. Maier, W. Ecker, J. Vila-Comamala, C. David, S. Schoeder, M. Burghammer*, X-ray nanodiffraction reveals strain and microstructure evolution in nanocrystalline thin films, Scr. Mater. 67 (2012) 748–751

57 *R. A. Young*, The Rietveld Method, Oxford University Press, Oxford 1993

58 *H. M. Rietveld*, The crystal structure of some alkaline earth metal uranates of the type M3UO6, Acta Cryst. 20 (1966) 508–513

59 *A. Albinati, B. T. M. Willis*, The Rietveld method in neutron and X-ray powder diffraction, J. Appl. Crystallogr. 15 (1982) 361–374

60 *G. Malmros, J. O. Thomas*, Least-squares structure refinement based on profile analysis of powder film intensity data measured on an automatic microdensitometer, J. Appl. Crystallogr. 10 (1977) 7–11

61 *G. Will*, Powder Diffraction, The Rietveld Method and the Two Stage Method to Determine and Refine Crystal Structures from Powder Diffraction Data, Springer-Verlag, Berlin 2006

62 *P. Scardi, L. Lutterotti, P. Maistrelli*, Experimental determination of the instrumental broadening in the Bragg–Brentano geometry, Powder Diffr. 9 (1994) 180–186

63 *L. B. McCusker, R. B. Dreele, D. E. Cox, D. Louër, P. Scardi*, Rietveld refinement guidelines, J. Appl. Crystallogr. 32 (1999) 36–50

64 *R. A. Young, D. B. Wiles*, Profile shape functions in Rietveld refinements, J. Appl. Crystallogr. 15 (1982) 430–438

65 *G. Caglioti, A. Paoletti, F. P. Ricci*, Choice of collimators for a crystal spectrometer for neutron diffraction, Nuclear Instruments 3 (1958) 223–228

66 *C. P. Khattak, D. E. Cox*, Profile analysis of X-ray powder diffractometer data: structural refinement of $La_{0.75}Sr_{0.25}CrO_3$, J. Appl. Crystallogr. 10 (1977) 405–411

67 *R. W. Cheary, A. Coelho*, A fundamental parameters approach to X-ray line-profile fitting, J. Appl. Crystallogr. 25 (1992) 109–121

68 *R. W. Cheary, A. Coelho, J. P. Cline*, Fundamental Parameters Line Profile Fitting in Laboratory Diffractometers, J. Res. Natl. Inst. Stand. Technol. 109 (2004) 1–25

69 *A. L. Ortiz, F. L. Cumbrera, F. Sánchez-Bajo, F. Guiberteau, R. Caruso*, Fundamental parameters approach in the Rietveld method: a study of the stability of results versus the accuracy of the instrumental profile, J. Eur. Ceram. Soc. 20 (2000) 1845–1851

70 *A. A. Coelho*, Whole-profile structure solution from powder diffraction data using simulated annealing, J. Appl. Crystallogr. 33 (2000) 899–908

71 *B. H. Toby*, R factors in Rietveld analysis: How good is good enough?, Powder Diffr. 21 (2006) 67–70

72 *E. Jansen, W. Schäfer, G. Will*, R values in analysis of powder diffraction data using Rietveld refinement, J. Appl. Crystallogr. 27 (1994) 492–496

73 NIST accessed Standard Reference Material 660c, 29 October 2015, www-s.nist.gov/srmors/view_detail.cfm?srm=660c

74 *J. W. Arblaster*, Crystallographic Properties of Platinum, Platin. Met. Rev. 50 (2006) 118–119

75 *J. W. Arblaster*, Crystallographic Properties of Platinum, Platin. Met. Rev. 41 (1997) 12–21

76 *H. Altun, S. Sen*, The effect of PVD coatings on the wear behaviour of magnesium alloys, Mater. Charact. 58 (2007) 917–921

77 Instruction Manual - HTK 1200N High-Temperature Oven-Chamber with CCU 1000 Control Unit, Document number: B40IB006EN-B, Anton Paar GmbH, Graz 2017

78 Instruction Manual - HTK 1200N Capillary Extension, Document number: B40IB005EN-E, Anton Paar GmbH, Graz 2017

79 *W. Martienssen, H. Warlimont*, Springer Handbook of Condensed Matter and Materials Data, Springer, Berlin 2005

80 *Y. hua Zhu*, General Rule of Phase Decomposition in Zn-Al Based Alloys (II) -On Effects of External Stresses on Phase Transformation-, Mater. Trans. 45 (2004) 3083–3097

81 *J. H. Perepezko, M. J. Uttormark*, Undercooling and Nucleation during Solidification, ISIJ Int. 35 (1995) 580–588

82 *A. M. Molodets, S. S. Nabatov*, Thermodynamic potentials, diagram of state, and phase transitions of tin on shock compression, High Temp. 38 (2000) 715–721

83 *S. Roberts, P. J. Dobson*, Evidence for reaction at the Al-SiO2 interface, J. Phys. D: Appl. Phys. 14 (1981) 17-22

84 *M. Stüber, H. Leiste, S. Ulrich, H. Holleck, D. Schild*, Microstructure and properties of low friction TiC-C nanocomposite coatings deposited by magnetron sputtering, Surf. Coat. Technol. 150 (2002) 218–226

85 *R. Bertoncello, A. Casagrande, M. Casarin, A. Glisenti, E. Lanzoni, L. Mirenghi, E. Tondello*, TiN, TiC and Ti(C,N) film characterization and its relationship to tribological behaviour, Surf. Interface Anal. 18 (1992) 525–531

86 *L. Xiaowei, R. Jean-Charles, Y. Suyuan*, Effect of temperature on graphite oxidation behavior, Nucl. Eng. Des. 227 (2004) 273–280

87 *P. Bhattacharya, P. Bellon, R. S. Averback, S. J. Hales*, Nanocrystalline TiAl powders synthesized by high-energy ball milling: effects of milling parameters on yield and contamination, J. Alloy. Compd. 368 (2004) 187–196

88 *L. G. Van Uitert, H. M. O'Bryan, M. E. Lines, H. J. Guggenheim, G. Zydzig*, Thermal expansion - an empirical correlation, Mat. Res. Bull. 12 (1977) 261–268